Anti-Icing Properties of Diamond Surfaces

Ida Pernille Løvås

Master Thesis in Physics:
Measurement Technology and Nanophysics

Department of Physics and Technology
University of Bergen

June 2022

Abstract

Ice formation causes significant problems in many outdoor infrastructure facilities operating in cold regions, such as power transmission lines, aircraft, wind turbines, optical sensors, and offshore operations. Current strategies involve melting, breaking, or chemical de-icing of already-formed ice. However, these techniques are often expensive and impractical due to their energy, time consumption, and design complexity. An anti-icing surface that prevents ice from forming and adhering to it without any additional energy is thus highly desirable. Several approaches have been suggested, often with the ground of superhydrophobic surfaces, which have been proven less robust in high humidity environments. Another approach with excellent anti-icing properties is nanostructured surfaces.

This thesis presents an investigation of the anti-icing properties of diamond surfaces with ultra-nano, nano, and micrometer roughness. The hardness, optical transparency, and wear-resistance of diamond make it suitable for coatings. Anti-icing properties of the surfaces were studied through water contact angles, freezing onset temperatures, and freezing delay times. Lastly, the results were compared to studies done by Eberle et al. [1], who found that nanostructured surfaces lead to the same low freezing onset temperature of approximately $-24\,^{\circ}\mathrm{C}$ for various surface roughness.

The diamond surfaces presented in this thesis show excellent anti-icing properties, with a freezing onset temperature of approximately $-22\,^{\circ}\mathrm{C}$ for both the ultra-nano, nano, and microstructured surfaces at a relative humidity of 20-40 %. The nanocrystalline samples also exhibit the same low freezing onset temperature for measurements done in a closed system, supporting the experiments by Eberle et al. [1].

However, at higher humidity (50-70 %), the freezing onset temperatures increases, with a variation depending on the roughness of the samples. The nanocrystalline diamond samples still exhibit great anti-icing properties with a freezing onset of $-18\,^{\circ}\mathrm{C}$ to $-21\,^{\circ}\mathrm{C}$ for the smoothest nanocrystalline samples. In contrast, the ultra-nanocrystalline and microcrystalline samples were more affected by the humidity conditions with a freezing onset of $-16\pm2\,^{\circ}\mathrm{C}$ and $-12\pm2\,^{\circ}\mathrm{C}$, given respectively.

Acknowledgement

Foremost, I would like to express my great appreciation to my supervisor, professor Bodil Holst of the Department of Physics and Technology at the University of Bergen, and my co-supervisor PhD-candidate Espen Werdal Selfors.

Thank you, Bodil, for giving me the opportunity to work on this project and for your encouragement and excellent guidance through this thesis. And Espen for all the help and guidance at the laboratory. Thank you both for the discussions, feedback, and suggestions at our meetings.

I would also like to thank Dr. Ranveig Flatabø for helping me with the AFM analysis.

A special thanks go to my precious Kanthee Kosolyuthasarn for always supporting and encouraging me to do my best. Thank you for always brightening my day and for the love you give me.

I would also like to express my gratitude to my fellow master's students and friends for the motivation and good conversations throughout this last year. Last but not least, I would like to thank my family for their support and encouragement.

Contents

Acronyms

ACA **A**dvancing **C**ontact **A**ngle.

CA **C**ontact **A**ngle.

CAH **C**ontact **A**ngle **H**ysteresis.

CVD Chemical Vapor Deposition.

MCD Microcrystalline Diamond.

NCD Nanocrystalline Diamond.

RCA **R**eceding **C**ontact **A**ngle.

RMS Root Mean Square.

UNCD Ultra-Nanocrystalline Diamond.

Chapter 1

Introduction

Ice formation on surfaces is commonplace in cold regions, affecting outdoor infrastructures, such as power transmission lines [2], aircraft [3], wind turbines [4], and offshore operations [5], see figure 1.1. Therefore, an anti-icing strategy is crucial for many applications as ice buildup can cause significant problems, safety risks, product breakage, or additional expenses. The leading solution has been an active anti-icing method, which involves removing ice after formation [6, 7]. Current ice-removal strategies involve melting, breaking, or chemical de-icing of already-formed ice layers [2]. These techniques are often expensive and impractical due to their energy, time consumption, and design complexity [2]. Passive anti-icing strategies involve methods that prevent ice from forming or adhering to a surface without additional energy power input [8]. Passive anti-icing strategies have become more attractive in the research community over the last years, mainly due to the huge scientific advances in the development of nano/microstructured surfaces and coating with tailored properties [8, 9].

Figure 1.1: Ice formation and buildup affect many outdoor infrastructures, which remains a huge problem. Image copied from [10].

It was first speculated that surfaces that strongly repel water, so called superhydrophobic surfaces, would also have anti-icing properties. Alizadeh et al. [11] demonstrated significant delay on superhydrophobic surfaces at low humidity ($<5\,\%$). However, in

contrast, Varanasi et al. [12] showed that superhydrophobic surfaces became more ice friendly at relatively high humidity due to condensation and frost formation. Additionally, Cao et al. [13] found that the anti-icing properties of a surface were not only correlated to superhydrophobicity but also depended on the roughness of the surface, explained by the classical nucleation theory (described in section 2.2.1).

Thus a better understanding of the effect of roughness on ice formation is needed, as studied by Eberle et al. [1]. They found that nanostructured surfaces exhibit excellent anti-icing properties, with the same great result for a range of different surface roughness in the nanoscale range. This will be discussed in more detail in section 2.2.3.

1.1 Anti-Icing Properties

The term *icephobic* has been established to describe these anti-icing surfaces that prevent ice from forming or adhering to it [14]. The icephobic or anti-icing properties of a surface can be characterized by the following:

1. Low median nucleation temperature, also called freezing onset temperature, T_N, defined as the temperature ice starts to nucleate in a water droplet placed on a surface when the entire system is cooled down [10].
2. Long average ice nucleation delay time (freezing delay time) τ_{av}, (given in section 2.2.2), defined as the average time required for ice to nucleate in a supercooled droplet when the droplet is maintained at thermal equilibrium with its surroundings [10].
3. Low ice adhesion strength, defined as a measure of how strong the bond between two surfaces is [15]. It is desirable, so already formed ice on a surface can easily be removed. [10]

1.2 Thesis Objectives

The specific objective of this thesis was to investigate the anti-icing properties of diamond surfaces, including:

- Analyze the AFM images of the diamond samples
- Measure the freezing onset temperature on each samples for various environment conditions. Including environment with relative humidity of 20-40 %, 40-50 %, 50-70 %, and saturated humidity (close to 100 %).
- Measure the freezing delay time on various subzero temperatures
- Investigate the wettabilities through static water contact angles and advancing and receding contact angles.
- Discuss how roughness affects anti-icing properties by comparing the result with experiments and proposed theory from Eberle et al. [1].

1.3 Thesis Outline

In order to develop an anti-icing surface, knowledge about wetting, icing, and surface topography is needed, which is given in the following chapters. Chapter 2 outlines the fundamental concepts of wetting and an introduction to the classical nucleation theory. It also discusses a proposed modification of the classical nucleation theory. Chapter 3 summarizes the diamond structure, followed by a description of the diamond coating growing process. Chapter 4 provides a brief overview of sample characterizations used in this thesis. The experimental procedure for this thesis work is given in chapter 5. Results and analysis of the experiments are provided in chapter 6 and discussed in chapter 7. Finally, a conclusion and suggestion for future work are presented in chapter 8

Chapter 2

Theory of Wetting and Nucleation

This chapter outlines the fundamental concepts of wetting on ideal and real surfaces. Then follows an introduction to the classical nucleation theory for ice formation on surfaces. Finally, the chapter introduces a reconsideration of the classical nucleation theory, which fits experimental results.

2.1 Wetting of Solid Surface

Wetting is the ability of a liquid to keep in contact with a solid surface, resulting from intermolecular interaction between the two interphases. Two main static scenarios can happen when a liquid drop is deposited onto a solid surface. Either the liquid spreads out completely, or the liquid forms a "cap" (droplet) sticking to the surface, as shown in figure 2.1. [16]

The wettability of a surface can be described according to the shape the liquid forms, determined by the tangential angle at the three-phase solid-liquid-vapor interface, known as the static contact angle [17]. The precise definition of the contact angle, which is illustrated in figure 2.1, is given in section 2.1.1.

The contact angle determines the surface area covered by a droplet (a given amount of liquid), which increases as the contact angle decreases and further increases wetting. Based on the value, contact angle θ indicates if the surface favors wetting or not. Figure 2.2 shows the different wettability surfaces can have. Surfaces are defined as hydrophilic when the contact angle is below 90° and indicates partial wetting. Surfaces with values below 5° are called superhydrophilic, complete wetting is observed when the contact angle equals zero. Surfaces above 90° are hydrophobic and correspond to partial non-wetting. Surfaces that hardly wet are called superhydrophobic and have contact angles greater than 150°. In the limit with contact angle 180°, we have complete non-wetting.

[18]

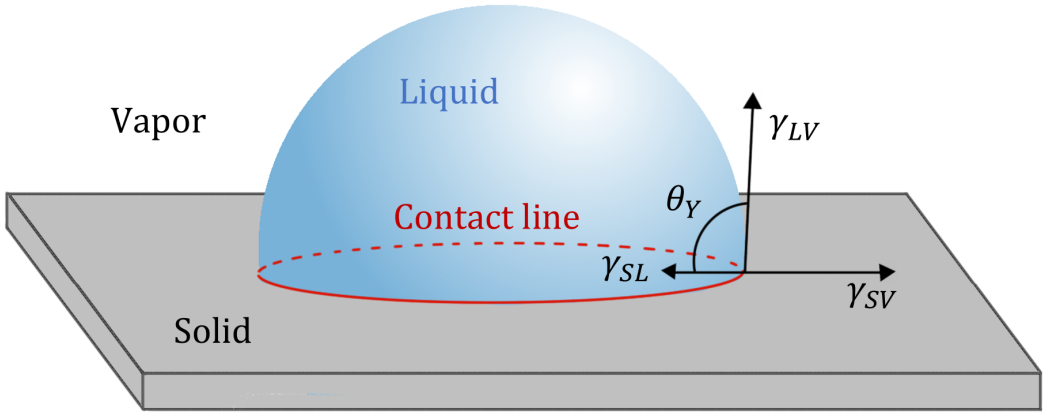

Figure 2.1: A droplet on an ideal solid surface. Young contact angle, θ_Y, is determined by the three surface tensions, solid-liquid γ_{SL}, solid-vapor γ_{SV}, and liquid-vapor γ_{LV}, at the three-phase contact line.

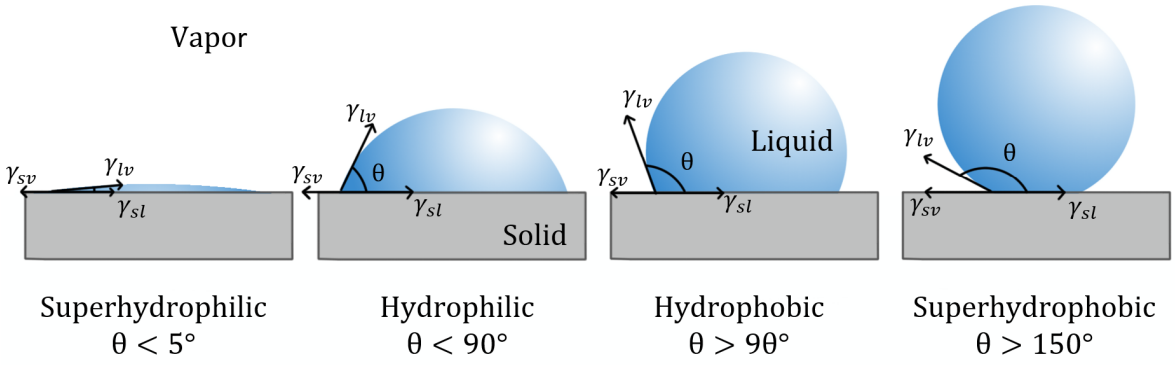

Figure 2.2: Different wettability surfaces can have, with good to poor wetting from left to right.

Theoretically, wetting of a surface can be calculated by using the interfacial and surface tension in the solid-liquid-vapor interface. This is described in section 2.1.1. It can also be experimentally measured through water contact angle experiments, see section 5.3. Reproducible and accurate contact angle measurements are crucial for analyzing surface wetting behavior. [19]

2.1.1 Liquid-Solid Interaction and Young Equation

As a liquid maintains contact with a solid surface, three interfaces exist solid-liquid, liquid-vapor, and solid-vapor interfaces, which all have their interfacial energy. This

interfacial energy or tension is due to an unbalanced distribution of forces at the interphase compared to the forces in the bulk phase, see figure 2.3. It is defined as the work, W, required to bring molecules from the bulk phase to its surface to increase the surface area A. Surface energy is often used instead of interfacial energy if the interface is a solid or liquid in contact with air. [18]

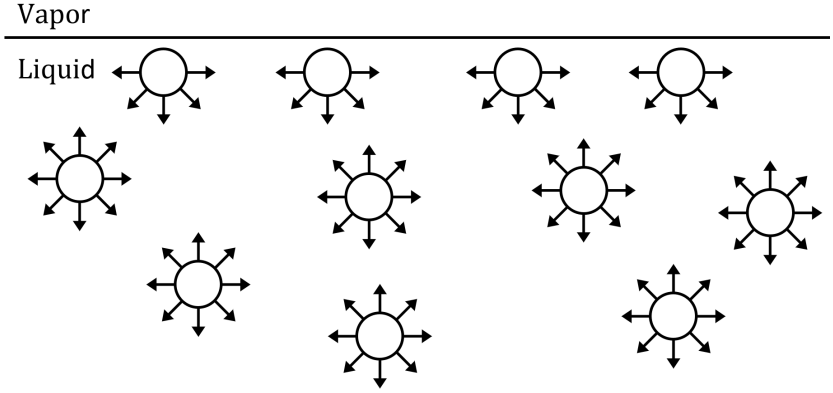

Figure 2.3: Concept of surface tension and its origin due to the molecules at the surface misses some of its interaction compared to the molecules in the bulk liquid.

The change in the total surface energy of the system, ΔE, can be expressed in terms of the change in surface area ΔA and contact angle θ, as follow [20]:

$$\Delta E = \Delta A(\gamma_{SL} - \gamma_{SV}) + \Delta A\gamma_{LV} cos(\theta - \Delta\theta) \tag{2.1}$$

where γ_{SL}, γ_{SV}, and γ_{LV} are the solid-liquid, solid-vapor, and liquid-vapor interfacial energies, respectively. The vectors of the surface energies are shown in figure 2.1.

As the system approaches equilibrium, the surface energy E is minimum, and change in surface area approaches 0, thus:

$$\lim_{\Delta A \to 0} \frac{\Delta E}{\Delta A} = 0 \tag{2.2}$$

Equation (2.1) then reduces to equation (2.3) known as the Young equation [21], which relates the contact angle only by the three interfacial energies [20].

$$cos\theta_Y = \frac{(\gamma_{sv} - \gamma_{sl})}{\gamma_{lv}} \tag{2.3}$$

where θ_Y is the Young equilibrium contact angle.

2.1.2 Wetting States

The Young equation is only valid for smooth, ideal solid surfaces. Real surfaces are more complex; they are often geometrically or chemically heterogeneous and rough [18]. Wetting of real surface can be divided into homogeneous and heterogeneous wetting regimes, described mainly by the two models, Wenzel and Cassie-Baxter state [22]. The homogeneous wetting regime is when liquid thoroughly wets into the surface's roughness, and the heterogeneous wetting regime is where air bubbles are trapped underneath the liquid, creating a composite interface [23]. For real surfaces, the wettability is characterized by an apparent contact angle and can be predicted by the Wenzel and Cassie-Baxter models [16]. Although, these models are only valid if the liquid drop is much larger than the surface roughness or heterogeneity [16].

Wenzel Approach

The relationship between roughness and wettability was first described by Wenzel [24], who assumed that the liquid penetrates the grooves, wetting every area of the rough surface under the liquid drop, as seen in figure 2.4. The model describes the homogeneous wetting regime. Wenzel distinguished the difference between the total or actual surface of an interface and the apparent surface, as illustrated in figure 2.4. He then modified Young's equation to account for the roughness effect: [22]

$$cos\theta_W = R_f \, cos\theta_Y \tag{2.4}$$

where θ_W is the Wenzel apparent contact angle on a rough surface, θ_Y the Young contact angle on an ideal smooth surface of the same material, and R_f the roughness factor given as:

$$R_f = \frac{\text{actual surface}}{\text{apparent surface}} \tag{2.5}$$

which gives $R_f = 1$ for smooth surfaces (reducing Wenzel eq to Young's eq) and $R_f > 1$ for rough surfaces. Wenzel equation hence states that wettability increases by roughness for hydrophilic surfaces because $\theta_W < \theta_Y$ and lowers for hydrophobic surfaces, $\theta_W > \theta_Y$ [22]. In other words, hydrophilic surfaces become more hydrophilic and hydrophobic more hydrophobic by adding roughness to the surface.

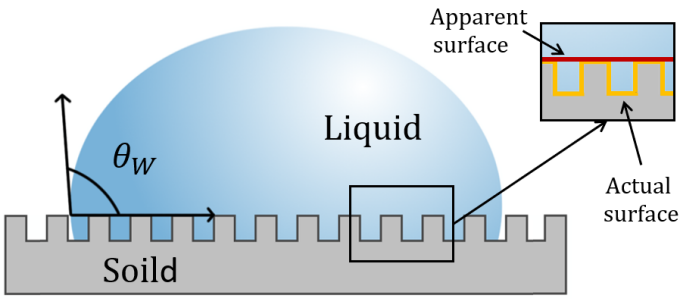

Figure 2.4: A liquid wetting solid surface according to the Wenzel model. θ_W is the apparent Wenzel contact angle. In the inset the difference between the apparent surface (red line) and the actual surface (yellow line) of an interface is shown

Cassie-Baxter Approach

However, the Wenzel equation is based on the assumption that the surface gets fully wetted. While under some circumstances, vapor pockets may be trapped underneath the liquid yielding a composite interface, as seen in figure 2.5. The Cassie-Baxter [25] model describes this heterogeneous wetting regime.

For a composite interface the Cassie equation was developed to describe heterogeneous surfaces with different chemistries [16]:

$$cos\theta_C = \sum f_i cos\theta_{Y,i} \tag{2.6}$$

where f is the area fraction characterized by the given chemistry and subscripts i indicate the different surface chemistries.

For a two-component surface composited of solid and vapor trapped in between the roughness, the equation becomes

$$cos\theta_{C-B} = f_S cos\theta_{Y,S} + f_V cos\theta_{Y,V} \tag{2.7}$$

where θ_{C-B} is the Cassie-Baxter apparent contact angle, $\theta_{Y,S}$ and $\theta_{Y,V}$ are the Young contact angles of a smooth surface of the same material at the solid-water and water-vapor interface. f_S and f_V are the surface and vapor area fractions. The Cassie-Baxter model assumes that $\theta_{Y,V} = 180°$. And since $f_S + f_V = 1$ equation (2.7) can be reduced to the Cassie-Baxter equation [22]:

$$cos\theta_{C-B} = f_S(cos\theta_{Y,S} + 1) - 1 \tag{2.8}$$

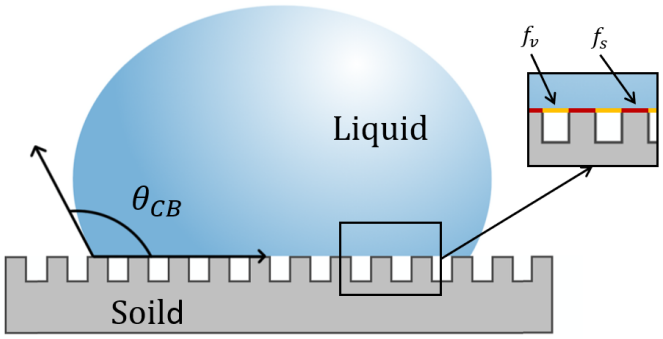

Figure 2.5: A Liquid wetting solid surface according to the Cassie-Baxter model. θ_{CB} is the apparent Cassie-Baxter contact angle. In the inset the surface area f_s (red line) and the vapor area f_v (yellow line) are shown.

2.1.3 Contact Angle Hysteresis

According to Young's equation (2.3), there is only one contact angle θ. However, experiments show that droplets on a surface have a spectrum of contact angles [22]. The Young equation presumes that the droplet is in a global energy minimum and, therefore, in a stable state corresponding to the Young contact angle [26], as seen in figure 2.6a. However, this equation is based on the assumption that the surface is smooth and heterogeneous. Real systems are more complex as drops can be in any local energy minimum within a spectrum of contact angles ranging from the so-called advancing contact angle θ_A up to the so-called receding contact angle θ_R [26]. Where the advancing contact angle (ACA) is the maximum and the receding contact angle (RCA) is the minimum value of the contact angles [22]. As seen in figure 2.6b, several local metastable contact angles exist. The difference between the ACA and the RCA is what we call contact-angle hysteresis (CAH) [26]:

$$H = (\theta_A - \theta_R) \tag{2.9}$$

The CAH is an evaluation of the mobility of the drop on a surface; the larger hysteresis, the less mobility the drop has [26]. It can be caused by contamination, roughness, and physical or chemical heterogeneity [18].

With current static contact angle characterization methods, it is not possible to know in which local metastable state within the hysteresis the static drop is. Therefore, the static contact angle measurements are not necessarily reproducible due to the hysteresis [26]. However, the ACA and the RCA are. Hence, these contact angles are essential to generate reproducible and meaningful contact angle data, as one static contact angle is less meaningful and only represents an angle somewhere between θ_A and θ_R [26, 27]. Therefore, in this thesis, measurements of the ACA and RCA, in addition to the static contact angle, are taken, see section 5.3.

The contact angle hysteresis can be measured by removing and adding liquid to the droplet. When increasing the drop volume, the contact line will remain fixed, and the contact angle of the drop increases until the ACA is reached. Further increase of drop volume will lead to movement of the contact line and increasing contact area while the contact angle remains constant. Conversely, by removing liquid from the drop, the contact line and contact area stay the same while the contact angle decreases until the RCA is reached. Further decrease of the volume will lead to movement of the contact line while the contact angle is constant. [26]

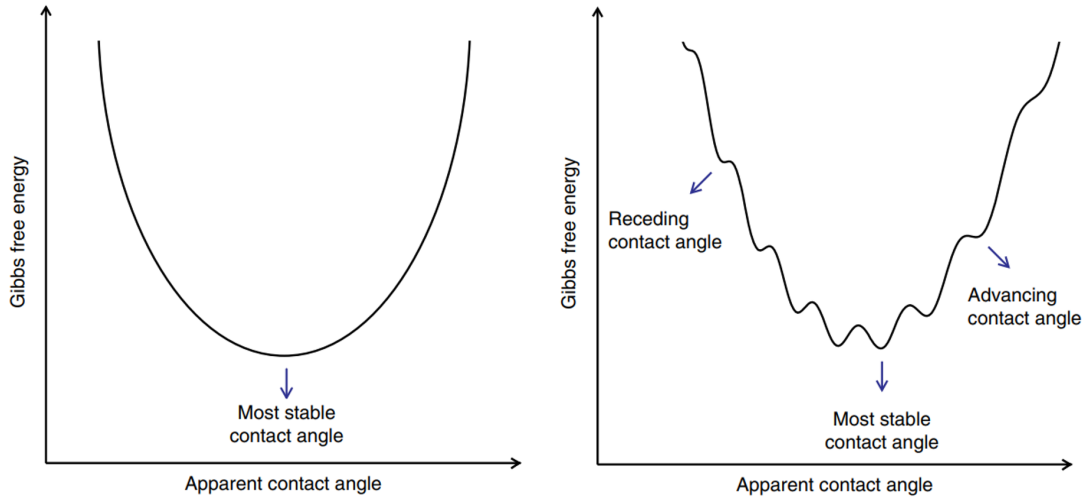

(a) An ideal wetting system with only one free energy minimum, corresponding to the most stable contact angle (Young contact angle).

(b) A real wetting system with the most stable contact angle at a global minimum and several local metastable static contact angles between the advancing and receding contact angle.

Figure 2.6: A sketch of Gibbs's free energy as a function of the apparent contact angle for an ideal and real wetting system. Illustration copied from [26].

2.2 Ice Nucleation

The Classical Nucleation Theory is the most common theoretical model used to explain the nucleation of new thermodynamic phases. It is an approximate theory that uses thermodynamics to predict nucleation rates. Originally it was based on vapor condensation to liquid but can be extended to other phase transitions. [28] This chapter will consider the transition from water to ice (liquid-solid transition).

As a thermodynamic system is about to undergo a phase transition, the first process is nucleation, forming a new phase in a metastable mother phase [29]. A metastable phase, in this case, a metastable liquid, is defined as a liquid placed out of an equilibrium state, such as a supercooled state below its thermodynamically freezing point [30]. The supercooled liquid will eventually transform into a stable or metastable solid phase at a given temperature and pressure. The transformation occurs due to the creation of

tiny clusters of the ice phase from the liquid phase by thermal fluctuations, called ice nuclei [31].

Ice nuclei can either nucleate through homogeneous or heterogeneous nucleation, depending on the presence of foreign bodies [32], as illustrated in figure 2.7. Homogeneous nucleation corresponds to the formation of nuclei within the liquid without pre-existing surfaces. If the nuclei are induced at the interface of a foreign body (dust particles, solid surface, etc.), the nucleation is heterogeneous. [28]

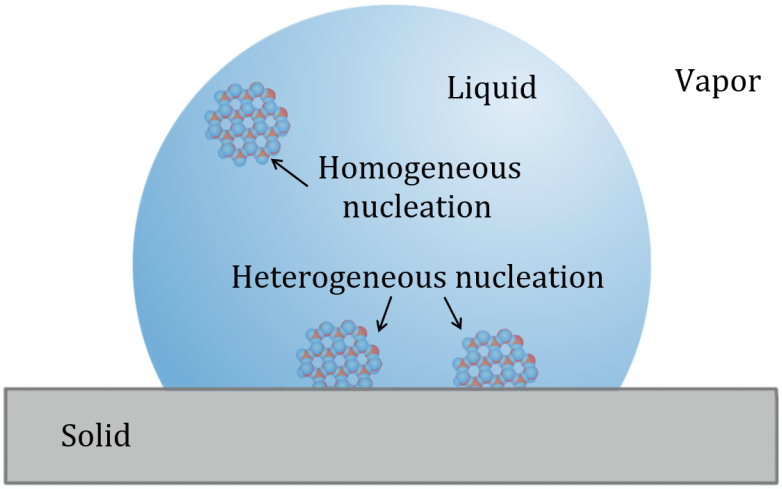

Figure 2.7: The illustration shows the different nuclei formations in a drop. The nuclei can either form within the liquid (homogeneous nucleation) or at the solid-liquid interface (heterogeneous nucleation).

2.2.1 Free Energy Barrier

As nucleation occurs, the system is put into a nonequilibrium metastable state [31]. As previously mentioned, it is achieved by cooling a liquid to a temperature below its freezing point. At this supercooled state the chemical potential of the new solid ice nuclei phase is lower than the liquid water phase, i.e., $\Delta\mu = \mu_{water} - \mu_{ice} > 0$ [33]. The chemical potential difference, $\Delta\mu$ of the system is the driving force for nucleation, which progressively widens as the system supercools and makes the system thermodynamically favorable to transform to the ice phase. [31, 34].

Physically the supercooled metastable state resembles a local minimum of the free energy, illustrated as state A in figure 2.8. It indicates that the system is stable for slight thermal fluctuations but eventually will evolve to state B in the figure, corresponding to a global minimum of the free energy. For the system to transition from state A to B, it must overcome a barrier. This barrier represents a local maximum of the free energy in figure 2.8, which corresponds to an unstable state. In order to overcome this energy

barrier, fluctuation is needed, which induces the formation of ice nuclei [31].

The formation of a new ice nucleus leads to a free energy loss of $-n\Delta\mu$, where n is the number of particles in the ice nucleus and $\Delta\mu$ is the change in chemical potential. Conversely, creating the phase boundary between the ice nucleus and the liquid with area A_I and interfacial energy γ_{WI} leads to a free energy gain of $A_I\gamma_{WI}$. [33]

The minimum work required to form an n-nucleus is equal to the change of the free energy, also called Gibbs free energy, ΔG, and is given as [31]:

$$\Delta G = -n\Delta\mu + \gamma_{WI}A_I \tag{2.10}$$

where n is the number of particles in the nucleus, $\Delta\mu$ is the chemical difference between the two phases, γ_{WI} is the water-ice interfacial energy, and A_I is the surface area of the ice nucleus. [31]

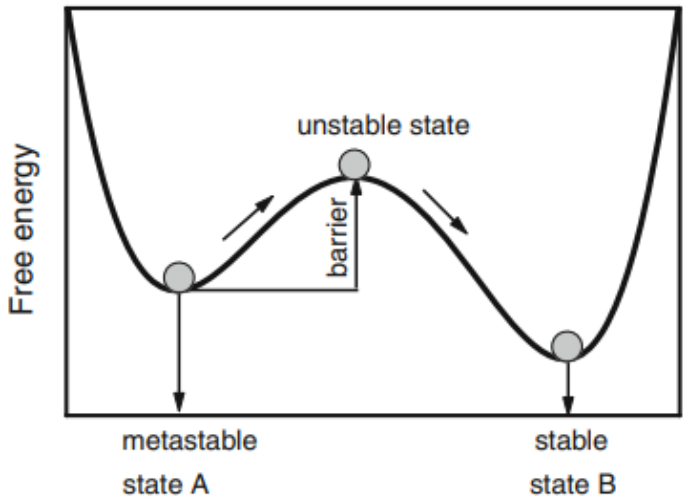

Figure 2.8: Illustration of the free energy of a system, where state A is a local minimum corresponding to a metastable state (supercooled liquid), and the global minimum state B corresponds to a stable state (ice). In order to transit from state A to B, the system must overcome the free energy barrier, represented by a global maximum. Illustration copied from [31].

Homogeneous Nucleation

Assuming that the ice nuclei are spherical with a radius r_n, then $A_I = 4\pi r_n^2$ and $n = \rho V = \frac{4}{3}\pi r_n^3\rho$, where ρ is the particle number density and V the volume of the nuclei. For homogeneous nucleation equation (2.10) can then be written as [31]:

$$\Delta G = -\frac{4}{3}\pi r_n^3\rho\Delta\mu + 4\pi r_n^2\gamma_{IW} \tag{2.11}$$

A plot of the Gibbs free energy ΔG with respect to the radius r_n is shown in figure 2.9. The first term of the equation represents the free energy of forming a new phase, which arises from bringing atoms or molecules together (blue line in figure 2.9). The second term represents the creation of a new interface (red line in figure 2.9). [34] For small r_n, the interfacial energy term dominates, increasing ΔG. As the radius grows, the volume energy term dominates, decreasing ΔG due to the energy decrease as the system transition from liquid to ice. The figure shows that ΔG reaches a maximum at a certain radius, called the critical nucleus radius. [28] To evaluate the critical nucleus radius, we require that:

$$(\frac{\delta G}{\delta r_n}) = 0 \tag{2.12}$$

which gives:

$$r^* = \frac{2\gamma_{IW}}{\rho \Delta \mu} \tag{2.13}$$

where r^* is the critical nucleus radius, which is the radius a nucleus must reach before freezing starts [1]. To reach r^* , the systems needs to overcome the energy barrier $\Delta G^*(r^*)$, which by substituting equation (2.13) into (2.11) is given as [31]:

$$\Delta G^*_{hom} = \frac{16\pi}{3} \frac{\gamma^3_{IW}}{(\rho \Delta \mu)^2} \tag{2.14}$$

Once the Gibbs free energy barrier, ΔG^*_{hom}, is overcome, the second stage of phase transition begins: growth [32].

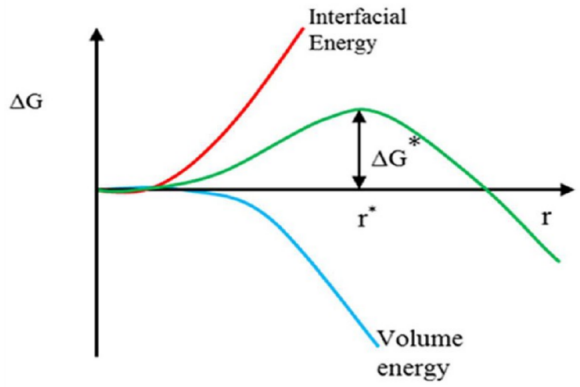

Figure 2.9: A plot of the Gibbs free energy (green line) as a function of ice nucleus radius. Gibbs free energy stems from the interfacial energy of creating a new interface (red line) and the volume energy of forming a new phase (blue line). Illustration copied from [28].

Heterogeneous Nucleation

For heterogeneous nucleation, nuclei grow onto a pre-existing surface (foreign-body, surface, dust, substrate, etc.), see figure 2.10. This is the situation investigated in the thesis, where we look at ice nucleation on different surfaces. In this case, the Gibbs free energy of forming a ice nucleus of radius r_n on a foreign body of radius R is given as [35]:

$$\Delta G = -n\Delta\mu + \gamma_{WI}A_{WI} + (\gamma_{SI} - \gamma_{SW})A_{SI} \tag{2.15}$$

where γ_{WI}, γ_{SI}, and γ_{SW} is the water-ice, solid-ice, and solid-water interfacial energy. A_{WI} and A_{SI} is the water-ice and solid-ice surface area. Solid is, in this case, used to denote the foreign particle or surface the ice nucleus is growing on.

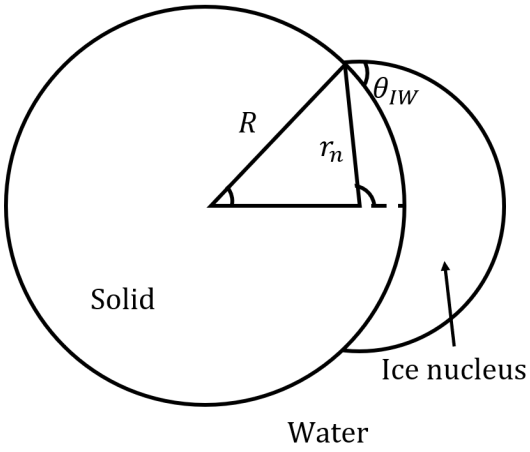

Figure 2.10: Ice nucleus of radius r_n nucleation onto a solid with radius R within water environment. θ_{IW} is the contact angle of the ice nucleus onto the solid surface.

By using trigonometry and referring to figure 2.10 an expression for the surface area A_{WI} and A_{SI} can be found [35]. By substituting these expressions into equation (2.15) and require that

$$(\frac{\delta G}{\delta r_n}) = 0 \tag{2.16}$$

the free energy barrier for heterogeneous nucleation can be expressed according to the homogeneous energy barrier as follow [32]:

$$\Delta G^*_{hetr} = \Delta G^*_{hom} f(m, x) \tag{2.17}$$

where $f(m, x)$ is called the Fletcher factor [35]. It has a value below unity and depends on the wetting characteristic and curvature of the nucleation site through the parameters m and x. Consequently, heterogeneous nucleation lowers the energy barrier compared to the homogeneous case due to the presence of foreign bodies, with the Fletcher factor being a measure of this reduction [31]. The parameter m is equal to the cosine of the ice nucleus contact angle, given as [36]:

$$m = \cos\theta_{IW} = \frac{\gamma_{SW} - \gamma_{SI}}{\gamma_{WI}} \tag{2.18}$$

where θ_{IW} is the contact angle of the ice nuclei in supercooled water on a solid. An illustration of this angle is shown in figure 2.11. γ_{SW}, γ_{SI} and γ_{WI} denotes the solid-water, solid-ice, and water-ice interface energies. The parameter x is the relative size of the solid with respect to the ice nucleus, given as [36]:

$$x = R/r^* \tag{2.19}$$

where r^* is the critical nucleus radius, and R is the curvature radius of the solid also referred to as the surface roughness radius, which corresponds to the radius R in figure 2.10.

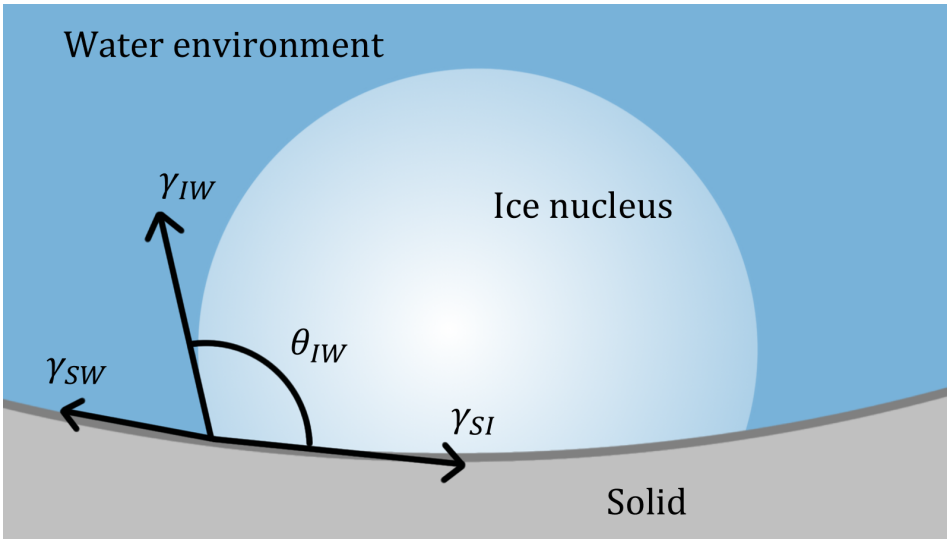

Figure 2.11: An ice nucleus within a water droplet at solid surface. θ_{IW} is the contact angle of the ice nucleus, and γ_{IW}, γ_{SW}, and γ_{SI} the ice-water, solid-water, and solid-ice interface energies.

Note that figure 2.10 only shows ice nucleus nucleate onto a solid with convex curvature. For a concave surface the trigonometry is different resulting in a different Fletcher factor. The Fletcher factor for nucleation on convex surface is given as [36]:

$$f_{\cap}(m,x) = \frac{1}{2}\left[1 - \left(\frac{1-mx}{g}\right)^3 + x^3\left[2 - 3\left(\frac{x-m}{g}\right) + \left(\frac{x-m}{g}\right)^3\right] + 3mx^2\left(\frac{x-m}{g} - 1\right)\right] \quad (2.20)$$

where

$$g = (1 + x^2 - 2mx)^{1/2} \quad (2.21)$$

And for concave curvature the Fletcher factor is [36]:

$$f_{\cup}(m,x) = \frac{1}{2}\left[1 - \left(\frac{1+mx}{g}\right)^3 - x^3\left[2 - 3\left(\frac{x+m}{g}\right) + \left(\frac{x+m}{g}\right)^3\right] + 3mx^2\left(\frac{x+m}{g} - 1\right)\right] \quad (2.22)$$

where

$$g = (1 + x^2 + 2mx)^{1/2} \quad (2.23)$$

The behavior of the Fletcher factor as a function of $x = R/r^*$ for various values of the ice-water contact angle θ_{IW} is shown in figure 2.12. Figure 2.12a shows the function for ice nuclei nucleation onto a surface with convex curvature (bump) and 2.12b onto a surface with concave curvature (pit). Each curve represents different contact angles of the ice nucleus, ranging from 180° to 18.2°. Both figures show that the curves start to level at $x = 10$. Therefore when $x > 10$, i.e., curvature radius $R > 10r^*$, the Fletcher factor is not affected by the curvature of the surface the ice nucleus is nucleation on, only the contact angle of the ice nucleus. However, the Fletcher factor is nonconstant when $x < 10$, i.e., when $R < 10r^*$. From figure 2.12a, the Fletcher factor decreases when R increases for convex curvature, meaning the flatter the convex bump gets, the smaller the Fletcher factor gets. And as seen in equation (2.17), the heterogeneous energy barrier, ΔG^*_{hetr}, is proportional to the Fletcher factor. Hence, bumps with curvature $R < 10r^*$, compared to a flat surface ($R = \infty$), suppress heterogeneous nucleation. The opposite is seen for concave curvatures in figure 2.12b, the Fletcher factor increases as the curvature radius R increases, meaning the flatter the pit gets, the higher the energy barrier gets. Hence, pits with curvature $R < 10r^*$ promote heterogeneous nucleation. Section 2.2.3 discusses how this is relevant for the surfaces investigated as part of this thesis work.

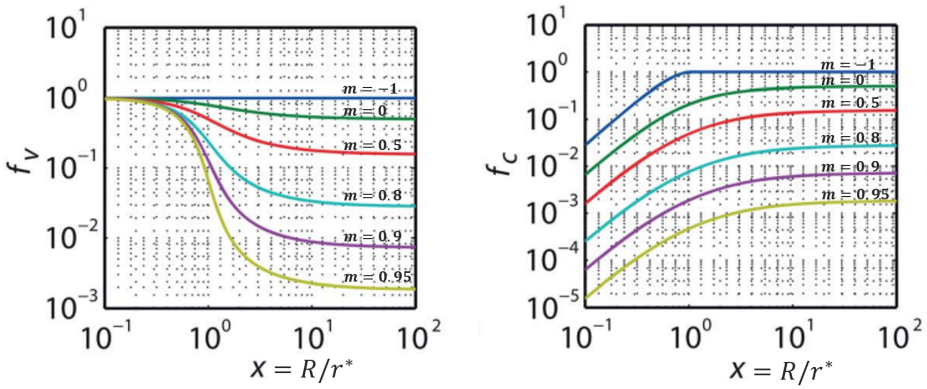

(a) Fletcher factor for convex curvature

(b) Fletcher factor for concave curvature

Figure 2.12: The Fletcher factor $f(x, m)$ plotted as a function of the ratio $x = R/r^*$ for (a) convex curvature and (b) concave curvature. Different curves are obtained with $m = \cos\theta_{WI} = -1, 0, 0.5, 0.8, 0.9, 0.95$ starting from the top, thereby spanning the contact angle θ_{IW} from 180° to 18.2°. Illustration copied from [1] and modified.

2.2.2 Ice Nucleation Rate

The nucleation rate, J, describes the number of nuclei growing to the critical radius r^* per unit volume, per unit time [29]. From the classical nucleation theory, the heterogeneous nucleation rate can be expressed as [31, 35]:

$$J(T) = J_0 e^{\frac{-\Delta G^*}{k_B T}} \tag{2.24}$$

where k_B is the Boltzmann constant, T is the temperature of supercooled water, ΔG^* is the heterogeneous free energy barrier given in section 2.2.1, and J_0 is a pre-exponential factor. The probability of an event occurring can be expressed through the Boltzmann distribution, which is proportional to the exponential of minus the free energy cost of the event over the thermal energy kT [37]. The exponential factor in equation (2.24) thus arises from the probability of forming a nucleus with radius r^*. The prefactor J_0 can be expressed as [10, 31]:

$$J_0 = Z(\nu A^*)N \tag{2.25}$$

with N being the number of atomic nucleation sites per unit volume, νA^* is the rate at which molecules stick to the critical nucleus causing it to grow, with ν called an impingement rate $[m^{-2}s^{-1}]$ and A^* the surface area of the critical ice nucleus $[m^2]$. However, for a nucleus in the critical region, there is a possibility that the nucleus will not overcome the energy barrier but dissociate into the liquid phase. The Zeldovich factor Z represents the probability of the nucleus crossing the energy barrier. [31]

From the nucleation rate, we can find the average ice nucleation delay time (or freezing delay time), which is the average time needed for a supercooled droplet to transform to ice when the droplet is maintained at thermal equilibrium with its surroundings. Given as: [10]

$$\tau_{av} = \frac{1}{J(T)} \tag{2.26}$$

Equation (2.24) implies that to prevent icing in a supercooled droplet on a surface, prefactor J_0 should be minimized, while the free energy barrier ΔG^* should be maximized. J_0 depends on the impingement rate ν and the contact area of the droplet through the number of nucleation sites available, N. ΔG^* can be altered through the ice-water contact angle θ_{IW} and the surface roughness R.

2.2.3 Roughness and Quasi-Liquid Layer

As mentioned in section 2.2.2, to suppress icing, the contact area A should be minimized, and ΔG should be maximized. ΔG_{hetr} can be altered through the ice-water contact angle θ_{IW} and the roughness curvature radius R of the surface, see equation (2.17). As discussed in section 2.2.1, convex bumps with curvature $R < 10r^*$ increase the energy barrier, while concave pits with curvature $R < 10r^*$ reduce the free energy barrier compared to a flat surface. All practical surface roughness constitutes bumps and pits simultaneously. Due to the very low Fletcher factor for concave pits, it dominates the freezing process. Hence, all surfaces with $R < 10r^*$ are expected to enhance ice nucleation.

However, the classic nucleation theory has not considered a possible quasi-liquid layer (i.e., a layer with reduced entropy and enhanced viscosity [38]) existing at the interface between the forming ice nucleus and the solid surface. The quasi-liquid layer was first postulated by Faraday [39] in 1859. Through a series of experiments on the adhesive properties of ice, he brought two ice balls together and observed a growth of a small bridge connecting them. As a result of his experiments, Faraday suggested that a quasi-liquid layer exists on the ice surface, even at temperatures well below freezing.[39] Figure 2.13 shows how the presence of such quasi-liquid layer leads to a change of θ_{IW} which will affect the free energy barrier ΔG.

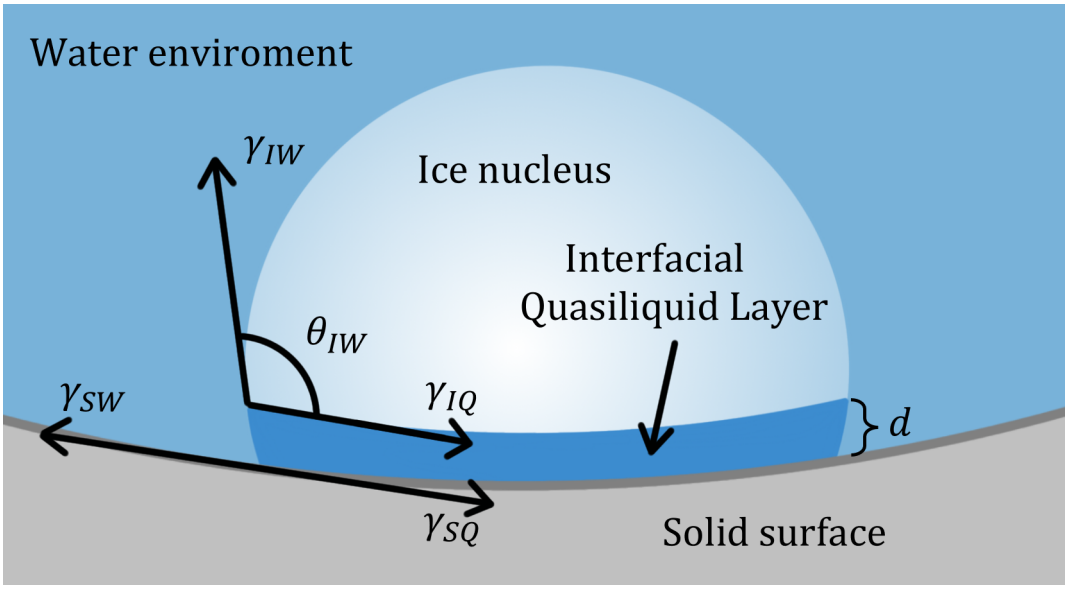

Figure 2.13: Ice nucleus formed in a nanopit with an quasi-liquid layer of thickness d. γ_{SQ}, γ_{SW}, γ_{IQ} and γ_{IW} is the surface-quasiliquid, surface-water, ice-quasiliquid and ice-water interfacial energies, and θ_{IW} the contact angle of the ice nucleus.

With the quasi-liquid presence, the interfacial energies of the system can then be balanced horizontally as follow [1]:

$$(\gamma_{SQ} - \gamma_{SW})\beta + \gamma_{IQ} + \gamma_{IW}\cos\theta_{IW} = 0 \tag{2.27}$$

where γ_{SQ}, γ_{SW}, γ_{IQ} and γ_{IW} is the solid-quasiliquid, solid-water, ice-quasiliquid and ice-water interfacial energies. β arises from the thickness d of the quasi-liquid layer and the surface roughness R, and is given as $\beta = \left(\frac{R}{R-d}\right)^2$. This gives a modified Young equation for the ice nucleus:

$$\cos\theta_{IW} = \frac{(\gamma_{SQ} - \gamma_{SW})}{\gamma_{IW}}\beta + \frac{\gamma_{IQ}}{\gamma_{IW}} \tag{2.28}$$

The solid-quasiliquid and ice-quasiliquid interfacial energies can be written as a function of the ice-water, solid-ice, and solid-water interfacial energies. The presence of a quasi-liquid layer will alter the surface energies. A surface will induce an ordering or disordering, which it will attempt to propagate into the bulk of which it forms the surface [40]. This effect will be screened by the quasi-liquid layer and is analogous to a screened potential. Using the screened potential decay of the interaction, the energy, due to a surface, at a distance, r from an area dA will be [40]:

$$dE \propto \frac{e^{-r/\xi}}{r} dA \tag{2.29}$$

where ξ is the scale length for the screening (i.e., the distance where the energy due to the surface is significantly reduced). Integrating the equation above gives the total contribution at a point due to a surface. For a flat surface, this integration gives $Ce^{\frac{-d}{\xi}}$, where C is a constant and d is the perpendicular distance from the surface. The total contribution to the energy due to a flat surface is then the integral over the volume of $Ce^{\frac{-d}{\xi}}$, plus a surface term [40]:

$$\begin{aligned} E_{surface} &= A\gamma^* + \int_0^t C_1 e^{\frac{-z_1}{\xi_1}} dV + \int_0^t C_2 e^{\frac{-z_2}{\xi_2}} dV \\ &= A\left[\gamma^* + C_1\xi_1(1 - e^{\frac{-d_1}{\xi_1}}) + C_2\xi_2(1 - e^{\frac{-d_2}{\xi_2}})\right] \end{aligned} \tag{2.30}$$

The subscripts 1's and 2's indicate which sides of the surface the volume is integrated over. For $d >> \xi$, the energy per unit area due to a surface is $\gamma_{1,2} = \gamma^*_{1,2} + C_1\xi_1 + C_2\xi_2$, which corresponds to measured surface energy one find in the literature. The limit of d going to 0 gives γ^*, which we will call the skin energy. [40]

We can now find the energy per area due to the non-interacting solid-quasiliquid and quasiliquid-ice surfaces with a distance d apart. Assuming that the bulk solid and ice thickness d_S and d_I is much larger than the scale length ξ of the screening through their bulk volume (i.e., $d_S >> \xi_S$ and $d_I >> \xi_I$). The energy per area is then given as:

$$E/A = \gamma^*_{SW} + \gamma^*_{IW} + C_{WS}\xi_W(1 - e^{-d/\xi_W}) + C_{SW}\xi_S + C_{WI}\xi_W(1 - e^{-d/\xi_W}) + C_{IW}\xi_I \tag{2.31}$$

If the distance between the surfaces is zero, the equation gives the solid-ice interfacial energy $\gamma_{SI} = \gamma^*_{SW} + \gamma^*_{IW} + C_{SW}\xi_S + C_{IW}\xi_I$. Letting d be large compared to the scale length ξ, the mismatch between the surface energies can be find by using the relation $\gamma_{1,2} = \gamma^*_{1,2} + C_1\xi_1 + C_2\xi_2$ [40]:

$$\begin{aligned} \Delta\gamma &= \gamma_{SI} - \gamma_{IW} - \gamma_{SW} \\ &= \gamma_{SI} - \gamma^*_{SW} - \gamma^*_{IW} - C_{WS}\xi_W - C_{SW}\xi_S + C_{WI}\xi_W - C_{IW}\xi_I \\ &= -(C_{WS}\xi_W + C_{WI}\xi_W) \end{aligned} \tag{2.32}$$

The energy per area of the two surfaces separated by a thickness d is then:

$$\begin{aligned} E/A &= \gamma_{SI} + C_{WS}\xi_W(1 - e^{-d/\xi_W}) + C_{WI}\xi_W(1 - e^{-d/\xi_W}) \\ &= \gamma_{SI} + (1 - e^{-d/\xi_W})(C_{WS}\xi_W + C_{WI}\xi_W) \\ &= \gamma_{SI} + (1 - e^{-d/\xi_W})(-\Delta\gamma) \\ &= \gamma_{SI} + (1 - e^{-d/\xi_W})(-\gamma_{SI} + \gamma_{IW} + \gamma_{SW}) \\ &= \gamma_{SI}e^{-d/\xi_W} + \gamma_{SW}(1 - e^{-d/\xi_W}) + \gamma_{IW}(1 - e^{-d/\xi_W}) \\ &= \gamma_{SQ} + \gamma_{IQ} \end{aligned} \tag{2.33}$$

By substituting $\gamma_{IQ} = \gamma_{IW}\left(1 - e^{\frac{-d}{\xi}}\right)$ and $\gamma_{SQ} = \gamma_{SI}e^{\frac{-d}{\xi}} + \gamma_{SW}\left(1 - e^{\frac{-d}{\xi}}\right)$ (let $\xi_W = \xi$), equation (2.28) can be written as [1]:

$$\cos\theta_{IW} = \beta\frac{(\gamma_{SW} - \gamma_{SI})}{\gamma_{IW}}e^{\frac{-d}{\xi}} + e^{\frac{-d}{\xi}} - 1 \tag{2.34}$$

For a flat surface ($R \to \infty$), $\beta = \lim_{R\to\infty}\left(\frac{R}{R-d}\right)^2 = \lim_{R\to\infty}\left(\frac{1}{1-\frac{d}{R}}\right)^2 = 1$. The contact angle for an ice nucleus with a quasi-liquid layer on a flat surface can be written as:

$$\cos\theta^*_{IW} = \frac{(\gamma_{SW} - \gamma_{SI})}{\gamma_{IW}}e^{\frac{-d^*}{\xi}} + e^{\frac{-d^*}{\xi}} - 1 \tag{2.35}$$

where θ^*_{IW}, d^* is the ice-water contact angle and thickness of the quasi-liquid layer on a flat surface. By substituting equation (2.35) in equation (2.34) one can write

$$\cos\theta_{IW} = (\cos\theta^*_{IW} + 1)\,\beta e^{\frac{-(d-d^*)}{\xi}} + (1 - \beta)e^{\frac{-d}{\xi}} - 1 \tag{2.36}$$

If one assume $R >> d$, then $\beta \approx 1$ and equation (2.36) can be rewritten as

$$\cos\theta_{IW} \approx (\cos(\theta_{IW})^* + 1)e^{\frac{-(d(R)-d^*)}{\xi}} - 1 \tag{2.37}$$

The presence of a quasi-liquid layer on ice nuclei forming in nanopits affects the ice-water contact angle θ_{IW}, which then depends on the thickness of the quasi-liquid layer d and the surface roughness R.

Experimental Observations Supporting the Quasi-Liquid Theory

Experimental observations from Eberle et al.[1] support the theory of a quasi-liquid layer at the interface between the ice nuclei and a surface. Eberle et al. [1] studied how nanostructuring would affect nucleation. To study how the surface roughness affects icing, they fabricated eighth hydrophobic nanotextured surfaces (labeled N1-N8) and three hydrophilic surfaces (labeled N9-N11) with different roughness. The RMS roughness (described in section 4.1.3) of the surfaces had a value ranging from 0.17-173 nm. The median nucleation temperature T_N (also referred to as the freezing onset temperature) was measured to study the samples' anti-icing characteristics. T_N refers to the temperature at which ice starts to nucleate in a water droplet placed onto a surface when the system is cooled down, see section 1.1. Their measurements were taken with saturated humidity with respect to ice to avoid any evaporation effects, corresponding to ∼100 % relative humidity. From Eberle et al. [1] experiments, they found that all samples lead to an extremely low nucleation temperature T_N of $\sim -24\,^{\circ}\mathrm{C}$ with very little change even with three orders of magnitude change in the RMS roughness. Their measured nucleation temperatures on the nanotextured samples are shown in figure 2.14, with each box summarizing 15-25 measurements.

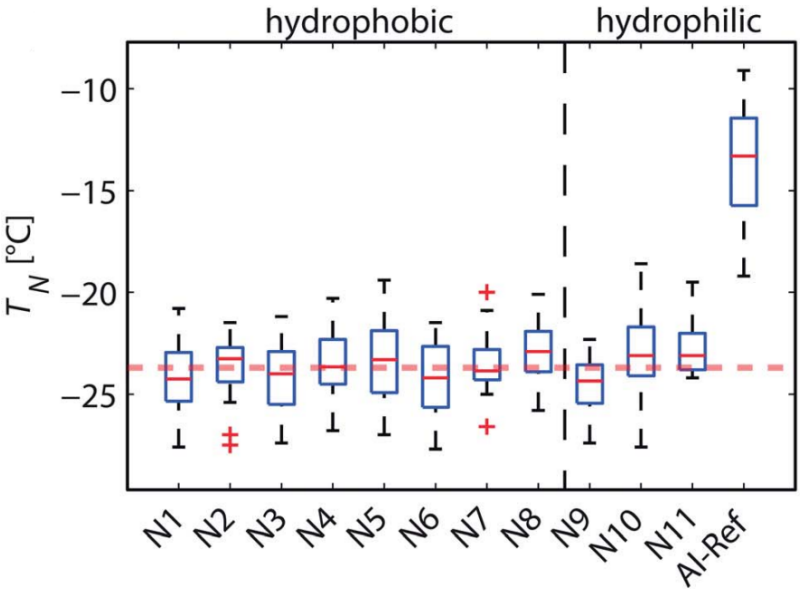

Figure 2.14: Results from Eberle et al. [1] experiments on the nucleation temperature for samples N1-N11 with different nanoscale roughness ranging from 0.17-173 nm. Including an aluminum substrate (Al-Ref) used for reference. The Red dashed line illustrates the nearly constant median T_N for all samples. The red line inside the boxes shows the median value for the sample. The box's bottom and top line represent the first and third quartile, which indicates where 25% and 75% of the data are below this point. Lower and upper whiskers are the minimum and maximum values. Any outliers are shown as red crosses.

As explained in section 2.2.1, starting from a flat surface, with a decrease in surface roughness R, convex nanobumps on a surface should, according to the classical nucle-

ation theory, suppress nucleation while concave nanopits should promote it. Therefore, when discussing the influence of nanotextured surfaces on ice nucleation, one should consider the presence and distribution of nanobumps and nanopits on the surface.

Figure 2.15a and 2.15b shows the surface texture and roughness curvature for samples N1 and N6, which Eberle et al. [1] found by using an atomic force microscope (AFM). Note that a surface typically has a distribution of R values with both nanopits and nanobumps; the curvature radius R is not simply the RMS roughness. The curvature radii values of one of the rougher samples, N6 (RMS roughness of $\sim 14.6\,\text{nm}$), were markedly smaller compared to the ultrasmooth substrate N1 (RMS roughness of $\sim 0.17\,\text{nm}$. The distribution of concave (pits) curvature radii sizes as a function of the area faction they occupy is shown in figure 2.15c and 2.15d. Eberle et al. [1] noticed that the radii of nanopits on N1 remain well above $10r^*$, while N6 had 15 % of its area occupied by nanopits with radii below $10r^*$. Thus, from the classical heterogeneous nucleation theory, they expected T_N to be substantially different on these surfaces (as nanopits promote nucleation with decreasing R, according to equation 2.22). However, their measurements on the surfaces N1-N11 show very little change in the nucleation temperature T_N for a broad range of RMS roughness, despite the presence of nanopits. This is highly desirable from a practical standpoint, as it allows fabricating a robust icephobic surface without requiring an ultraprecise tuning of the roughness.

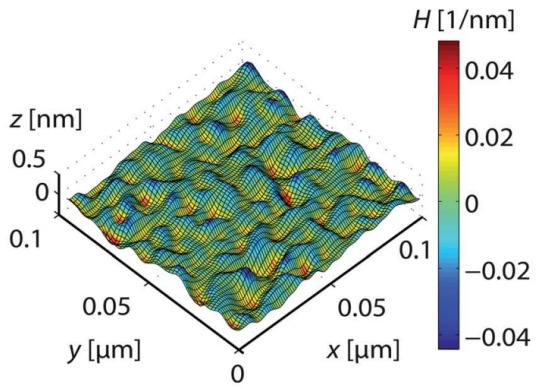

(a) The surfacetexture of sample N1 with RMS roughness ∼0.17 nm, obtained by AFM.

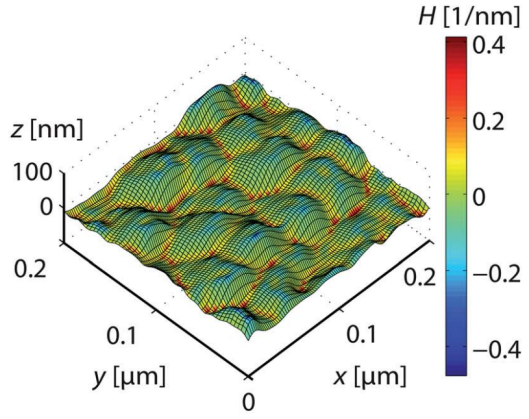

(b) The surface texture of sample N6 with RMS roughness ∼14.6 nm, obtained by AFM.

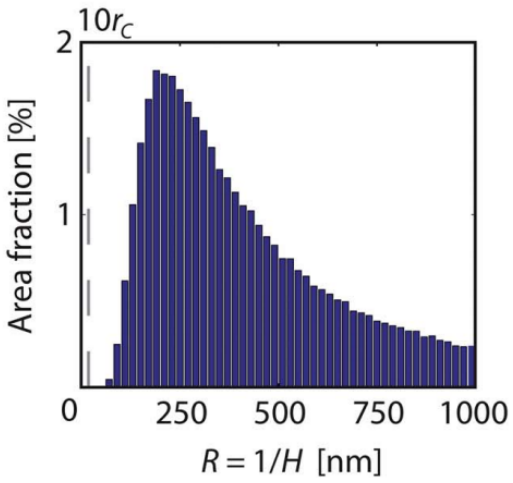

(c) The area fraction occupied by nanopits as a function of this curvature radius R for sample N1.

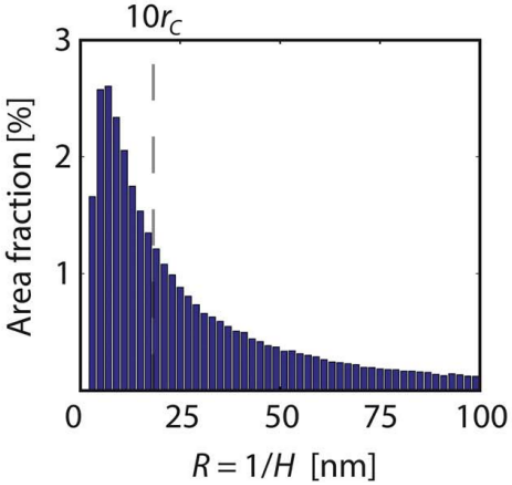

(d) he area fraction occupied by nanopits as a function of this curvature radius R for sample N6.

Figure 2.15: Surfacetexture and distribution of nanopits on samples N1 and N6 form Eberle et al. [1] experiments. Colors in **a)** and **b)** indicates the curvature H at a given point on the samples. For sample N1 the curvature radius $R = 1/H$ of the nanopits remains all over $10r^*$, see **c)**, while 15 % of the nanopits on N6 have a curvature radius smaller than $10r^*$.

Eberle et al. [1] proposed that the reason behind this minimal change in T_N is due to a quasi-liquid layer that alters the nucleation characteristics, as discussed in section 2.2.3. They refer to experiments and computational results that have confirmed the presence of a quasi-liquid layer at the ice-surface interface of a crystallized water cluster similar to ice nuclei in size. Thereby concluding that a quasi-liquid layer is also present between ice nuclei at their samples. The quasi-liquid layer causes a change of the ice nucleus contact angle θ_{IW}, see equation (2.37). The equation shows a dependence of θ_{IW} with the thickness of the quasi-liquid layer, which depends on the radius of curvature R.

In figure 2.16, Eberle et al. [1] plotted the expected change in the nucleation temperature T_N as a function of curvature radius R on the surface with 15 % of its area occupied

by concave nanopits. The blue dashed curve is obtained from the classical nucleation theory (without quasi-liquid layer) for a constant $\theta_{IW} = 100°$, which fails to predict their experimental results. The green dashed line in Figure 2.16 shows θ_{IW} given by equation (2.37) as function of the curvature radius R. This curve clearly shows that θ_{IW} increases with decreasing R. By account for the change in θ_{IW} due to the quasi-liquid layer, the obtained T_N from corrected nucleation theory becomes constant (solid black line in figure 2.16). This is in good agreement with their experiments. The change of θ_{IW} counteracts the roughness-dependent ice nucleation promotion in nanopits. Hence, nucleation on flatter regions with $R > 10r^*$ becomes dominant. [1]

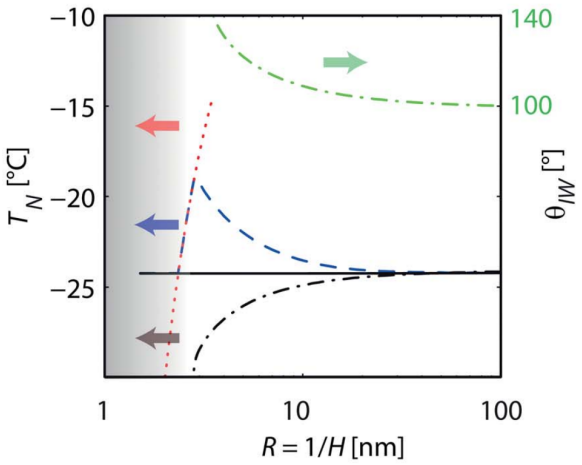

Figure 2.16: A plot of Eberle et al. [1] calculation of T_N from the nucleation theory as a function of roughness curvature radius R for a surface with 15 % of its area covered by nanopits. The blue dashed line shows results from the classical nucleation theory for constant $\theta_{IW} = 100$, and the solid black line for increasing θ_{IW} with decreasing R due to the quasi-liquid layer. The Green dashed line shows the dependency of the altered θ_{IW} with R. The black dashed line shows the T_N for a hypothetical surface with 100 % of its surface occupied by concave nanopits. The red dashed line shows the melting point depression curve.

Chapter 3

Micro-, Nano-, and Ultra-Nanocrystalline Diamond Coatings

This thesis investigates the anti-icing properties of diamond coatings; therefore, a brief overview of diamond coatings is needed. This chapter presents the structure of the diamond and its properties. Followed by a description of the growing process used in this thesis. Lastly, a description of micro-, nano-, and ultra-nanocrystalline diamond coatings.

3.1 Diamond Structure

Diamonds consist of carbon atoms, which have an atomic number of six, with four valence electrons (electrons in the outer shell). The electrons in an atom are found in a series of energy levels called orbitals, which only allows two electrons of opposite spin in each orbital. In the carbon atom, the inner electrons occupy the $1s$ orbital, and the valence electrons the $2s$ and $2p$ orbitals, which gives a ground-state (i.e., lowest possible energy state) electron configuration of $1s^2 2s^2 2p^2$. [41] Such configuration allows carbon to exist in several forms, known as allotropes, distinguished by their physical structure and orbital hybridization [42]. The most common allotropes of carbon are diamond and graphene. These structures have covalent bonding between the carbon atoms, i.e., the electrons are shared between neighboring carbon atoms [43]. Only the valence electrons are available for bonding to other atoms and can either form sp, sp^2 or sp^3 hybrid bonds [41].

In a sp^2 hybridization, the covalent bonds are constructed from one $2s$ orbital with two $2p$ orbitals forming three sp^2 hybrid bonds. This hybridization is found in graphene,

which forms a honeycomb lattice structure, as seen in figure 3.1a. The graphene structure is two-dimensional, which can be stacked together, forming a three-dimensional structure of weakly bonded graphene sheets called graphite, see figure 3.1b.

In the sp^3 hybridization, the bonds are constructed from one $2s$ orbital and three $2p$ orbitals. This results in four sp^3 hybrid bonds forming a tetrahedral configuration, which are found in diamonds. The diamond structure can also be described by a face-centered cubic lattice, as seen in the figure. [43] Unlike graphene, diamond is a three-dimensional structure, where each tetrahedron combines with four other tetrahedral to form a strongly bonded and entirely covalent crystalline structure. [41]

Due to the different hybrid bonds and structures, the properties of carbon allotropes vary widely. Diamond is, for instance, the hardest known material (thus exhibiting great wear resistance), while graphite can be one of the softest. Diamond is also transparent to the visible spectrum, while graphite is opaque. The hardness, optical transparency, and wear-resistance of diamond make it suitable for coatings. [41]

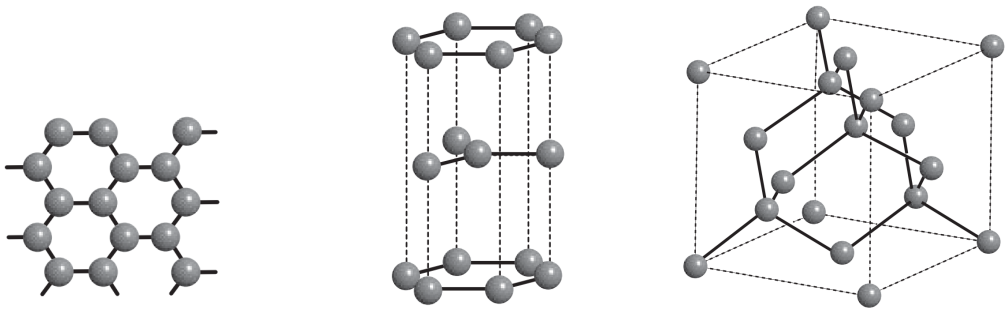

(a) Graphene is a two-dimensional structure consisting of sp^2 hybrid bonds.

(b) Graphite consisting of graphene sheets weakly bonded together to form a three-dimensional structure.

(c) Diamond structure consisting of sp^3 hybrid bonds that form a tetrahedron structure described by a face-centred cubic lattice.

Figure 3.1: Some of the most common carbon allotropes structures. Illustration copied from [43]

3.2 Growth of Diamond Films by Chemical Vapor Deposition

Chemical Vapour Deposition (CVD) is one of the methods widely used to grow diamonds as films or coatings on various substrates with high-quality [44, 45]. It involves depositing a solid product onto a heated substrate from a chemical reaction in the vapor phase in an activated environment (e.g., heat, light, or plasma) [46]. One of CVD's advantages is the ability to control the products' surface morphology and crystal structure by handling the CVD process parameters [47]. Moreover, the thin diamond film still offers many bulk diamond properties [44].

Nucleation is a fundamental process in diamond growth. However, it occurs with a very low probability on a non-diamond substrate [48]. Therefore, pretreatment of the substrate is always needed to enhance the nucleation density and grow a high-quality continuous diamond film [49]. Several pretreatments can be used, e.g., scratching or abrading the substrate with diamond paste. Due to the pretreatment, the remaining diamond seed acts as nucleation sites for diamond growth, enhancing the nucleation density. [49]

After the pretreatment step, the substrate is placed into a CVD chamber and exposed to reactant gases. When growing diamond films, the reactant gases consist of hydrogen and a carbon-containing gas. The carbon atom in the gas is used to form a diamond structure. However, at ambient temperatures and pressures, the stable form of solid carbon is graphite [50]. Therefore, the gas needs to be activated, or only graphite would be formed [41]. Several CVD techniques exist, and the fundamental difference in these techniques is how the gas phases are activated to form a stable solid diamond film. The primary CVD techniques are hot filament CVD and plasma CVD, shown in figure 3.2. [45]

The hot filament CVD method, illustrated in figure 3.2b, uses heated tungsten wires (filaments) to activate the reactant gases, typically in high temperatures (>900 °C). The plasma CVD method, illustrated in figure 3.2a, uses positively charged ions and negatively charged electrons (plasma) to activate the reactant gases. The plasma activation in CVD commonly uses a lower temperature than hot filament CVD, i.e., 300-500 °C. [46] Depending on the crystal structure and surface morphology, both methods can be used to grow diamond films. However, a temperature between 500 and 1200° is commonly used, as a temperature below or above this results in the growth of other carbon structures such as graphene [51].

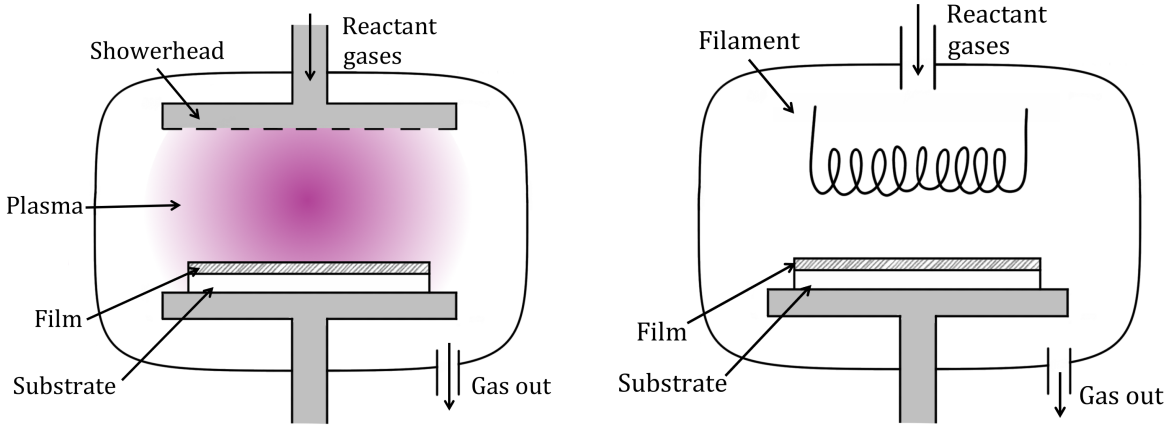

(a) Plasma CVD. Reactant gases are added to the chamber through a showerhead. Plasma (i.e., ions and electrons) activates the gases, causing the growth of a film on a substrate.

(b) Hot filament CVD. Reactant gases are added to the chamber, passing a hot filament that activates the gases and deposits a solid product onto a substrate creating a film.

Figure 3.2: Chemical vapor deposition techniques.

As mentioned above, the growth of CVD diamond requires hydrogen and carbon-containing gas. A highly diluted methane (CH_4) concentration in hydrogen is most commonly used, which reacts as follows when activated: [46]

$$CH_4(g) \rightarrow C(diamond) + 2H_2(g) \tag{3.1}$$

The hydrogen gas is also activated by the filament or plasma (depending on the CVD method used), which dissociates into atomic hydrogen as follows:

$$H_2 \rightarrow H + H \tag{3.2}$$

Figure 3.3 illustrates the reaction process in the CVD growth of diamond films. An explanation of each step in the figure is as follows:

1. The atomic hydrogen reacts and removes hydrogen from the carbon surface, leaving a reactive surface site behind.
2. Some of the atomic hydrogens also react with the source hydrocarbon (CH_4) and create a mixture of hydrocarbons. A hydrocarbon (CH_3) then collides and reacts with the surface site, adding another carbon to the surface.

3-4. This process may repeat at neighboring sites, adding more carbon to the structure.

5. Eventually, a hydrogen atom will abstract a hydrogen atom from the CH_3 group, creating a CH_2 group.

6-7. The CH_3 and CH_2 groups will attract and form a circular structure, locking the carbon atoms to the diamond surface.

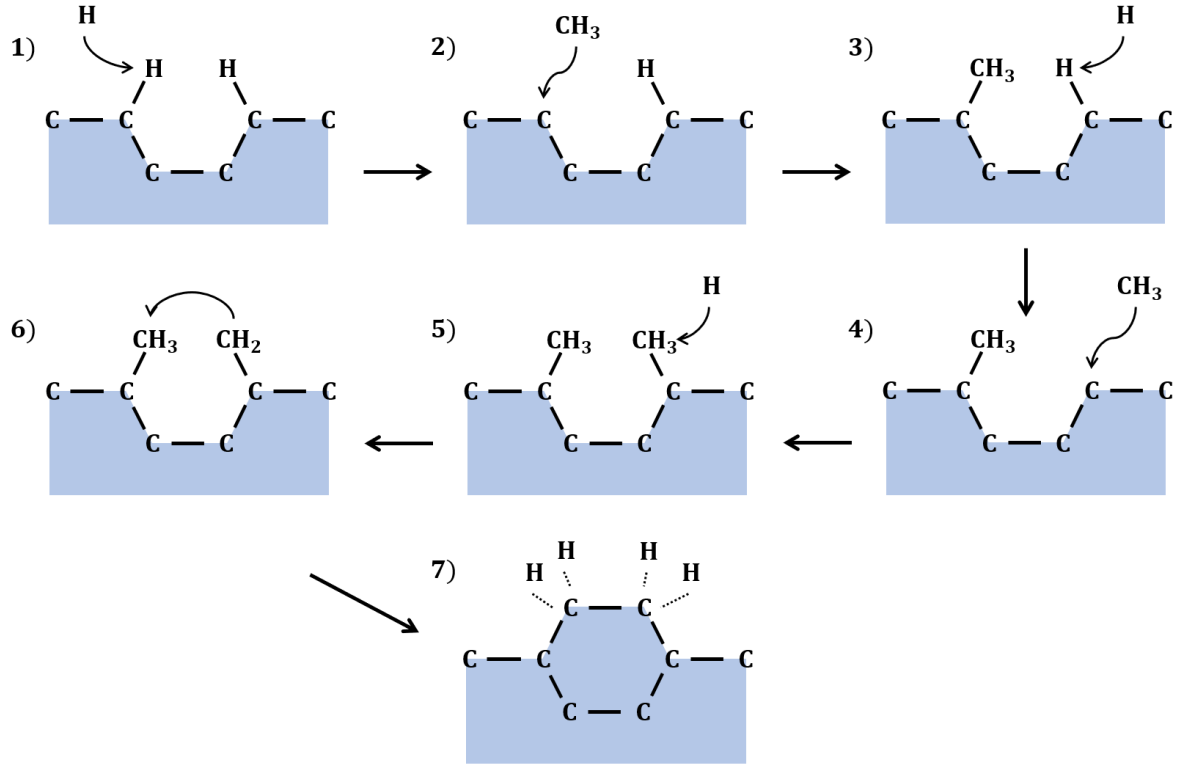

Figure 3.3: A schematic representation of the reactions occurring at a diamond surface causing it to grow. 1. Atomic hydrogen removes hydrogen from the carbon surface. 2. CH_3 reacts with the reactive surface site. 3-4. Reactions repeated at neighboring sites. 5. Hydrogen atom abstract hydrogen atom from CH_3 creating CH_2. 6-7. The hydrocarbons attract and create diamond structures.

3.2.1 Diamond as Coating Films

The term nanocrystalline diamond (NCD) has been used to describe diamond films with grain size less than 100 nm. Accordingly, the smallest grain size diamond films are called ultra-nanocrystalline diamonds (UNCD) with grain size smaller than 10 nm. The distinction in morphology originates from the growing process of the diamonds, primarily due to the hydrogen gas concentration used.

Graphene and other carbon structure may also form simultaneously with diamond growth. Thus the diamond film grown in CVD can consist of both sp and sp^2 carbon sites on the surface [44]. The sp^2 bonds allow a re-nucleation of diamond grains due to the formation of new nucleation sites. However, hydrogen atoms have a significantly higher etch rate of graphite (sp^2) over diamond (sp^3), and stabilize the diamond structure by hydrogen termination [44, 52]. Therefore a hydrogen-rich gas is critical for the CVD growth process of diamond films. It also reduces the re-nucleation of diamond grains, allowing the grains to grow from the seeded substrate to the film surface, as illustrated in figure 3.4a. This means that after the film has grown to a certain thickness, the grains will no longer be of nanometer scale. If the thickness is grown to a

micrometer scale, the film will be referred to as microcrystalline diamond (MCD). If the film is grown very thin and with a high nucleation density, NCD can be grown. [53]

The UNCD films are grown with re-nucleation, which is achieved by reducing the concentration of hydrogen in the growth process. This allows more sp^2 bonding to form and create new nucleation sites on parts of the crowing diamond grains, as illustrated in figure 3.4b. The continuous interruption of the grains growth results in a grain size limitation, meaning thick films can be grown with small grain sizes. It also means that the grain boundaries constitute a substantial part of the total material volume, which will affect the material properties. [53] E.g., due to less re-nucleation growth, NCD films contain less sp^2 bonds and are thus more transparent than UNCD films [44].

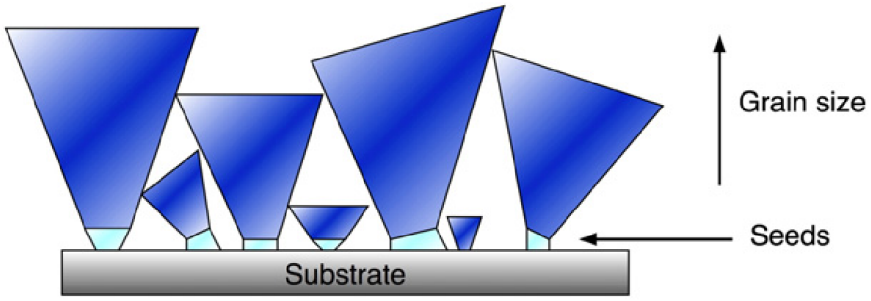

(a) Diamond film grown without re-nucleation allows the grains to grow from the substrate to the surface. Often found in nanocrystalline and microcrystalline diamonds.

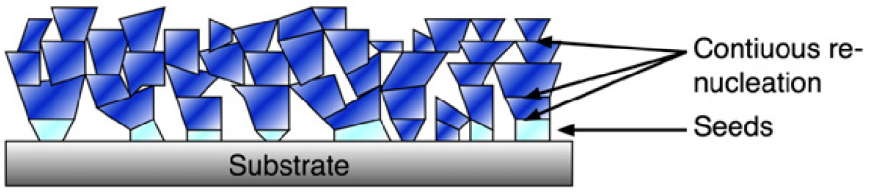

(b) Diamond film grown with re-nucleation limits the maximum grain size due to continuous interruption of the growth. Found in ultra-nanocrystalline diamonds.

Figure 3.4: Illustration of diamond film growth with and without re-nucleation of grains. Illustration copied from [53].

Chapter 4

Sample Characterization

This chapter provides a brief overview of Atomic Force Microscopy used to study the topography of the diamond surfaces.

4.1 Atomic Force Microscopy

Atomic Force Microscopy (AFM) is a technique that examines materials surfaces in a three-dimensional detail down to nanometer scale [54]. AFM aims to measure the force acting between a sample surface and a probe tip, scanning the surface to track the surface topography [55].

4.1.1 Basic Principles of AFM

In order to measure the surface topography, a very sharp tip is used to probe and map the surface. As the tip is brought close to the sample surface with a distance between them in the nanoscale range, near-field forces act between the tip and surface [56]. The AFM detects attractive and repulsive forces depending on how close the tip-sample distance is. For close distance, attractive forces are detected between the tip and surface, while if the tip is brought in contact or minimal distance apart, a strong repulsive force act between [55].

To detect the near-field forces acting between tip and sample, the AFM uses a microscopic force sensor. The most commonly used force sensor is a cantilever. The tip, used to probe the surface, is placed at the end of the cantilever, as seen in figure 4.1. As near-field forces act between the tip and surface, it causes the cantilever to bend elastically, which is detected using a beam-deflection method. As seen in figure 4.1, a laser beam is reflected at the back of the cantilever and directed and measured by

position-sensitive photodiodes. The elastic bending of the cantilever causes the laser beam to tilt and changes the striking position on the photodiodes. [57]

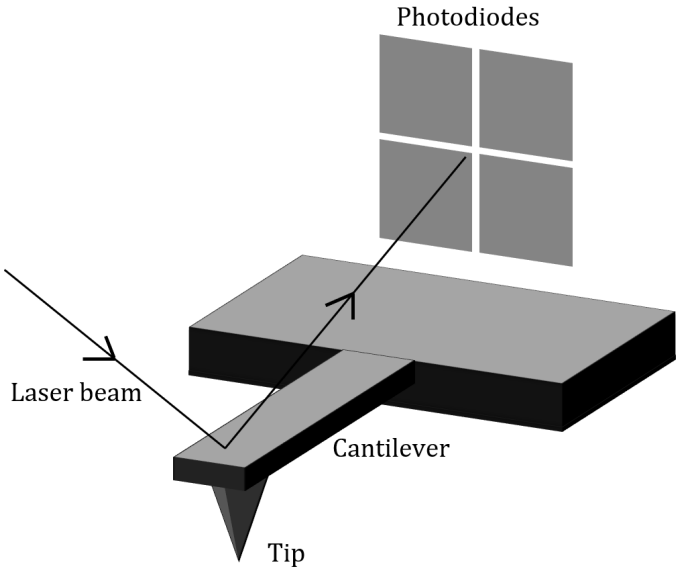

Figure 4.1: Cantilever force sensor for AFM, based on beam-deflection method. A laser beam is reflected at the cantilever and directed to position-sensitive photodiodes. Any deflection of the cantilever changes the striking positions on the photodiodes.

4.1.2 Operation Modes

The AFM has several operational modes, divided into static mode - constant deflecting of the cantilever, and dynamic mode - oscillating cantilever [57].

Static mode

In the static mode, often called static contact mode, the tip is brought in contact with the surface. In the most straightforward mode, the tip glides over the surface while measuring the tip's vertical movement as the cantilever bends due to the height variation on the surface. This mode is called the constant height mode. However, this mode can cause damage to the tip or sample due to high contact force upon the hills or the risk of losing contact in the deepest valleys. [54]

Instead of constant height, the AFM can use constant force between tip and sample during scanning, called the constant force mode, illustrated in figure 4.2. It uses a feedback loop that takes the cantilever deflection as input and uses it to correct the distance between the tip and sample surface to maintain a constant force between them. The vertical z displacement is then recorded as the surface height. [54]

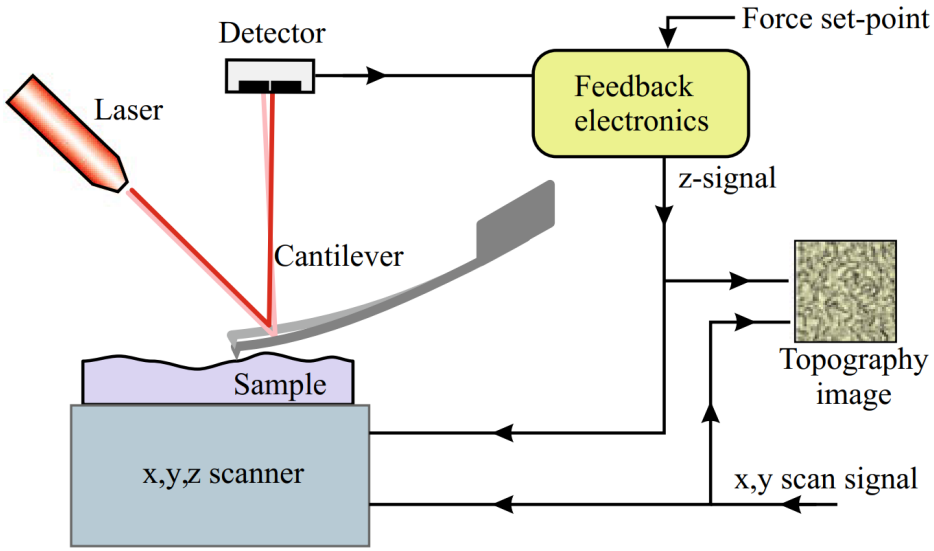

Figure 4.2: Illustrations of the static constant force AFM mode. The elastically bending of the cantilever is measured by a beam-deflection method. A feedback loop takes the deflection as input and uses it to correct the tip's distance to maintain a constant set-point force between tip and sample. The displacement of the vertical position (z-signal) is then recorded as the surface height at the given (x,y) position. Illustration copied from [55]

Dynamic Modes

Several dynamic modes have been developed to overcome the limits of the static contact mode [57], e.g., damage to the surface due to the tip being in contact with the sample (mostly on soft and fragile samples, such as biological samples) [55]. The dynamic modes consist of non-contacting and intermittent contact (tapping mode), which uses an oscillating cantilever. In the non-contact mode, the vibrating tip is brought near the sample surface without touching it. Interacting forces between the tip and sample shift the cantilever's oscillation frequency. This frequency shift is used to maintain the tip-sample distance through a feedback loop. The non-contact mode is operated in the attractive force regime, meaning weak attractive forces interacts between the tip and sample instead of strong repulsive forces in contact mode. [55]

In tapping mode, the cantilever oscillates near the surface while the tip lightly touches it before raising the tip to avoid any surface damage. The cantilever oscillation amplitude is reduced due to an energy loss when the tip is in contact with the surface. This reduction in amplitude compared to the free-oscillation state is used to measure the surface topography. The feedback loop uses this reduction to control the tip-sample distance to maintain the oscillation frequency. [57]

4.1.3 Data Analysis

Many image analysis methods can be done with the AFM data, often very specific to the problem under investigation. In this thesis, the AFM images are analyzed to measure the roughness of the surface. One of the parameters commonly used to describe the roughness characteristic of a surface is the Root Mean Square (RMS) roughness R_{RMS}. The RMS roughness is defined as the standard deviation of the surface heights $h(x, y)$ on the sample, given as: [55]

$$R_{RMS} = \sqrt{\frac{1}{N}\sum_{i=1}^{N}\left(h_i\left(x,y\right) - \overline{h}\right)^2} \tag{4.1}$$

with N being the total number of pixels in the image and $\overline{h}$ the average surface height.

Chapter 5

Methods

This chapter describes the experimental procedure for this thesis work, including freezing and wetting experiments. The anti-icing properties of the samples were investigated through freezing experiments, including measurements of the freezing onset temperature and the freezing onset delay times. Wetting properties of the samples were investigated through water contact angles (WCA) measurements and the contact angle hysteresis by measuring the advancing and receding contact angle (ACA and RCA).

5.1 Equipment

An optical contact angle instrument Dataphysics OCA 20, was used for the wetting and freezing experiments, shown in figure 5.1 and schematically illustrated in figure 5.2. The instrument consists of a high-speed camera (red part in the figure 5.2), a temperature-controlled stage and a water cooling device (green part), and a motorized syringe for precisely controlling the volume of the deposited drop (blue part). The data analysis was performed using the SCA 20 software for the instrument.

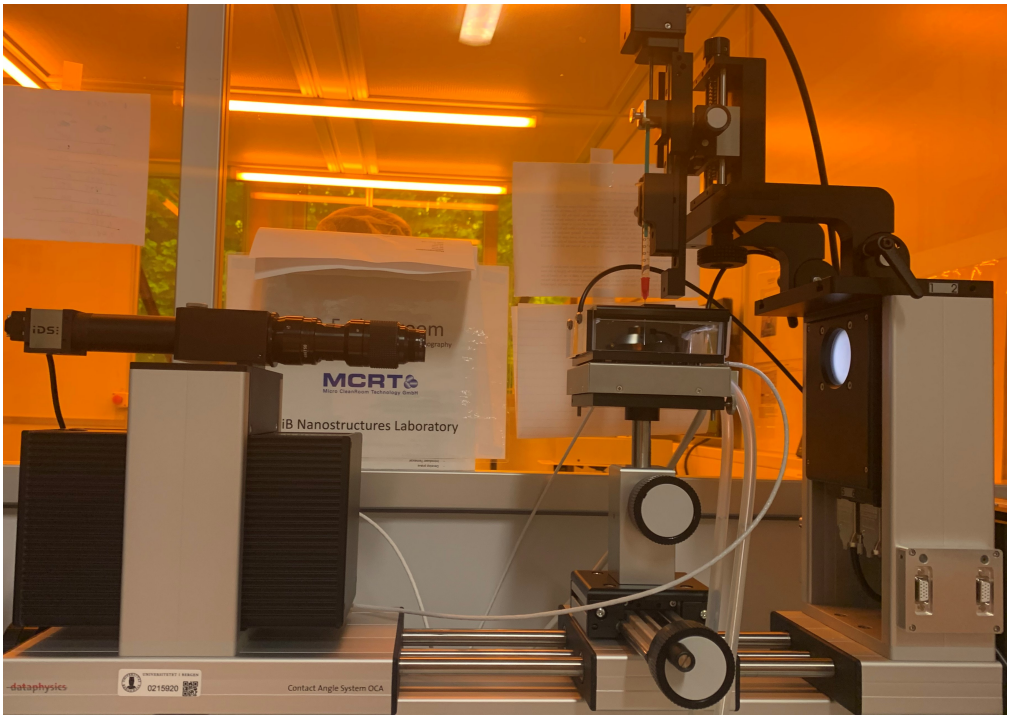

Figure 5.1: The optical contact angle instrument Dataphysics OCA 20 used in this thesis.

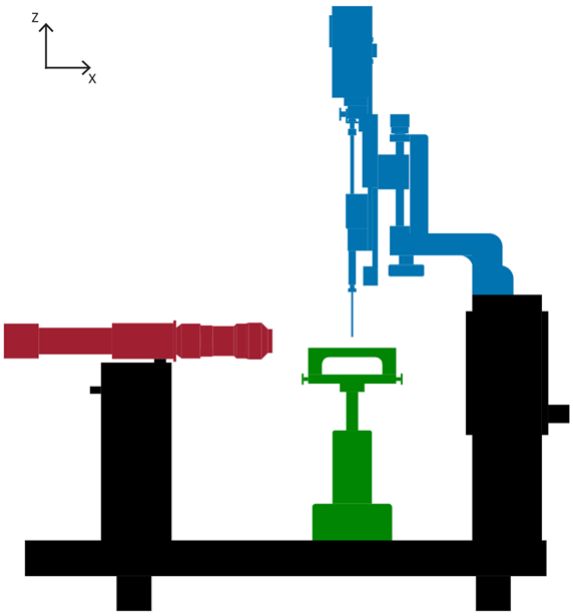

Figure 5.2: Schematic illustration of the optical contact angle instrument used. The instrument consists of a high-speed camera (red part), a sample stage (green part), and a motorized syringe (blue part). Copied from [58]

All measurements were done in a cleanroom to prevent dust adsorbing on the sample or water droplet and impacting the measurements. The room temperature and relative humidity in the room were reported during each experiment. In some experiments, an environmental chamber was used, shown in figure 5.3. The right side image shows the chamber closed with a lid, allowing only a tiny hole for the syringe needle to fit through. The environmental chamber's advantage is to ensure a constant atmosphere during the measurements, with a saturated humidity close to 100 %. The left image also shows the chamber, however, without the lid exposing the sample stage to the surrounding atmosphere in the room.

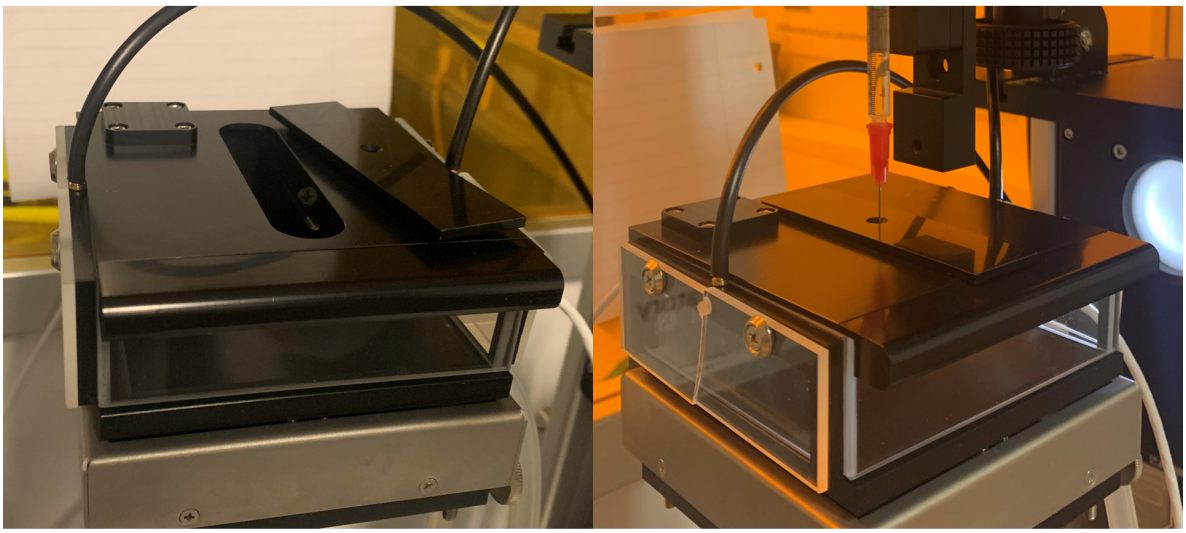

Figure 5.3: The environmental chamber used in this thesis. The left image shows the chamber with an open lid. And the right image with a closed box, with only a tiny hole for the needle.

Before starting the first experiments, the syringe was filled with new deionized water to avoid impurities that could alter the surface energy. The samples were cleaned using acetone and isopropanol, then dried with N_2.

5.2 Freezing Experiments

Before the experiments, the samples were prepared by cleaning the sample with acetone and isopropanol and then placed at the sample stage.

5.2.1 Freezing Onset Temperature Measurements

The freezing onset temperature measurements were done by cooling down the samples below subzero until the water droplet froze. The samples were placed on the cooling

stage. The environmental chamber was used for some measurements, creating a closed system with only a tiny hole for the syringe. For each measurement, a water droplet of 5 µL was deposited onto the sample surface at 23 °C. The cooling stage was cooled down at a constant rate of 0.16 °C s^{-1} until the droplet froze.

The freezing of a water droplet cooled down with the substrate it is placed on occurs in two freezing stages. In the first stage, the droplet heats up adiabatically from its supercooled temperature to its equilibrium temperature, resulting in a mixed liquid/solid phase in the entire droplet [9]. This first stage can be observed as a change in the optical appearance of the droplet where the droplet starts to appear hazy (as seen in the middle image in figure 5.4). The first freezing stage only takes a couple of milliseconds. A change in appearance was observed during experiments, and this was taken to be the freezing onset, i.e., the start of the freezing process. In the second slower freezing stage, isothermal freezing of the remaining liquid occurs [9] (seen in the right image in figure 5.4).

The freezing onset experiments were carried out in four cycles with 6-8 measurements for each sample. An average freezing onset temperature was then found. The position of the water droplet on the sample was varied for each measurement.

Before repeating the experiments, the sample was heated to 35 °C and the drop removed by a lint-free paper tissue. To ensure that all remaining water evaporated, the sample was left on 35 °C for 5 min before continuing. Lastly, a N_2-rinse to remove any dust particles.

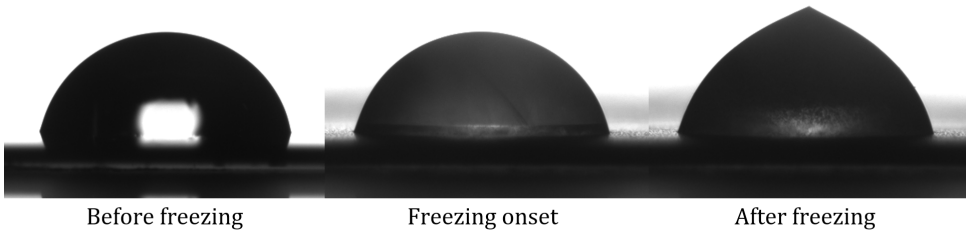

Figure 5.4: The freezing process of a 5 µL water drop on a surface. The left shows before freezing. The freezing process occurs in two stages. First, the droplet heats up adiabatically, resulting in a mixed liquid/solid phase in the entire droplet [9]. This is observed as the drop appears hazy, as seen in the middle image, which is the freezing onset. In the second stage, complete freezing of the remaining liquid occurs, as seen in the right image.

5.2.2 Freezing Delay Measurements

The freezing delay measurements were done by cooling the samples to a desired subzero temperature. The samples were placed on the cooling stage, and the environmental chamber was used. A water droplet of 5 µL was deposited onto the sample at 23 °C. The sample was then cooled at a rate of 0.16 °C s^{-1} down to either −5 °C, −10 °C, −15 °C or −20 °C. The time it took for freezing to begin after the sample had reached the selected subzero temperature was measured and referred to as the freezing delay time. The exact temperature of the cooling stage when cooled down fluctuated ±0.4 °C from the set subzero temperature before it stabilized.

After the experiments, the sample was heated to 35 °C, droplet removed by lint-free paper tissue, and waited for 5 min to give time for the remaining water to evaporate. A N_2-rinse then removed any dust particles.

5.3 Wetting Experiments

5.3.1 Water Contact Angle Measurements

Before every freezing onset measurement, the water contact angle (WCA) at room temperature was measured. A 5 µL droplet of water was deposited onto the sample, and the CA was measured using the instrument's software as described in section 5.3.2. The WCA for each sample was calculated as an average of 6-8 measurements.

5.3.2 Advancing and Receding Contact Angle Measurements

As mentioned in section 2.1.3, measurement of a static contact angle is not necessarily reproducible due to CA hysteresis. However, the advancing and receding contact angles (ACA and RCA) are. They are measured by recording a video while increasing and decreasing the drop volume (see figure 5.6). As the volume is increased, the CA will increase while the contact line remains stable until ACA is reached (fig. 5.6a-c). As the droplet has reached its highest CA (known as the ACA), further increase of the volume will lead to movement of the contact line while the CA stays ideally constant (fig. 5.6c).

Before the experiments, the samples were prepared by cleaning the sample with acetone and isopropanol and then placed at the sample stage. Measurements of the ACA and RCA were performed following the procedure given by [26], which uses the so-called sessile-drop (needle in) method. Measurement of the advancing contact angle was done as follows [26]:

1. 2 µL of water was dispensed and carefully placed onto the sample surface. The needle was left halfway inside the drop, in the middle of the drop.
2. Dispensed 1 µL of water at a flow rate of 0.05 µL s^{-1}. The overall size was then 3 µL.

! Low flow rate is necessary to avoid dynamic effects.

3. Waited for 30 s to make sure the system was in equilibrium.
4. Started recording a video. Then quickly continued to the next step.
5. Dispensed 8 µL water at a flow rate of 0.05 µL.

! Was cautious not to cause any disturbance during this phase as it could cause dynamic effects.

6. The video was stopped, and the recorded images were used for analyzing the ACA.

For RCA measurements, the drop volume is decreased, as seen in figure 5.6. At first, as the volume decreases, the shape of the droplet will change while the contact line will remain the same until RCA is reached (fig. 5.6d). As the RCA (the lowest CA) is reached, further decreasing the volume leads to movement of the contact line while the CA remains stable (fig. 5.6e). The drop will eventually be distorted by the needle when the volume becomes too small. Thus, the initial drop volume must be large enough to reach RCA before the drop becomes distorted. By estimating the ACA and RCA of the samples, a recommended starting volume for RCA measurements can be determined by figure 5.5. Before starting, a test measurement was done to find the approximate RCA, so the recommended starting volume could be chosen. The RCA measurements were then done as follows [26]:

1. The drop volume was increased to the desired volume.
2. The needle was adjusted, if needed, so it was close to the sample surface without toughing it. Also, made sure the needle was still in the middle of the drop.
3. Removed water from the drop at a flow rate of 2 µL until the volume was ∼13 µL. Adjusted needle again if needed.
4. Removed 2 µL at 0.05 µL s^{-1}. The overall drop volume was then ∼11 µL.
5. Waited for 30 s to make sure that the system was in equilibrium
6. Started recording a video. Then quickly continued to the next step.
7. Withdrew water at a flow rate of 0.05 µL until the drop was completely removed.
8. Stopped the video. The recorded images were used for analyzing the RCA.

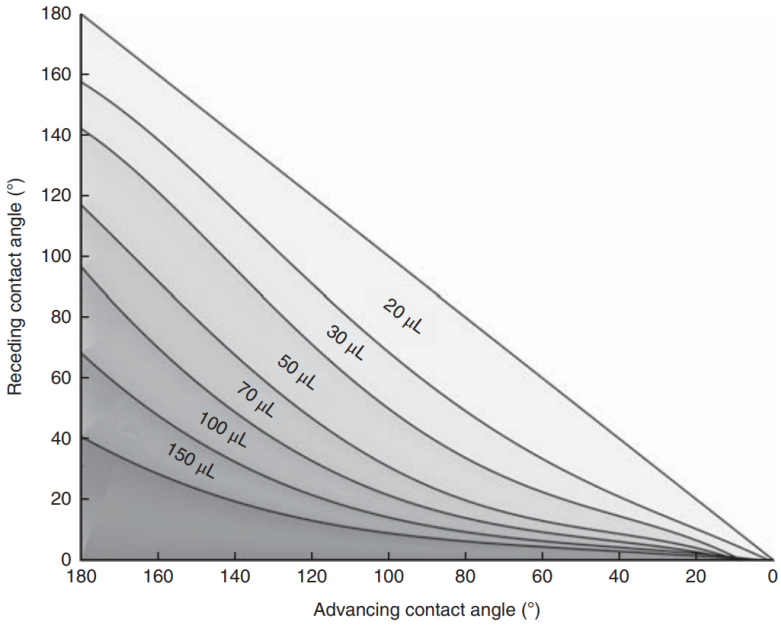

Figure 5.5: Recommended starting volume for RCA measurements to reach RCA at 10 µL. By using an estimate of the ACA and RCA of the sample to be measured the starting volume can be determined from plot. The figure is copied from [26].

The videos were then analyzed using the software-operated fitting procedure to determine the profile of the droplet. Before the curve fitting can be performed, the baseline, the contact line between the solid-liquid-gas interface, must be determined. The baseline was either placed automatically or manually. All the recorded images could then be analyzed to find the CA based on the curve of the drop profile. By plotting the baseline length and CA as a function of time, ACA can be found as an average of the CA when the baseline increases and RCA when the baseline decreases.

After each experiment, the remaining water was removed by a lint-free paper tissue followed by a N_2-rinse before repeating the experiments.

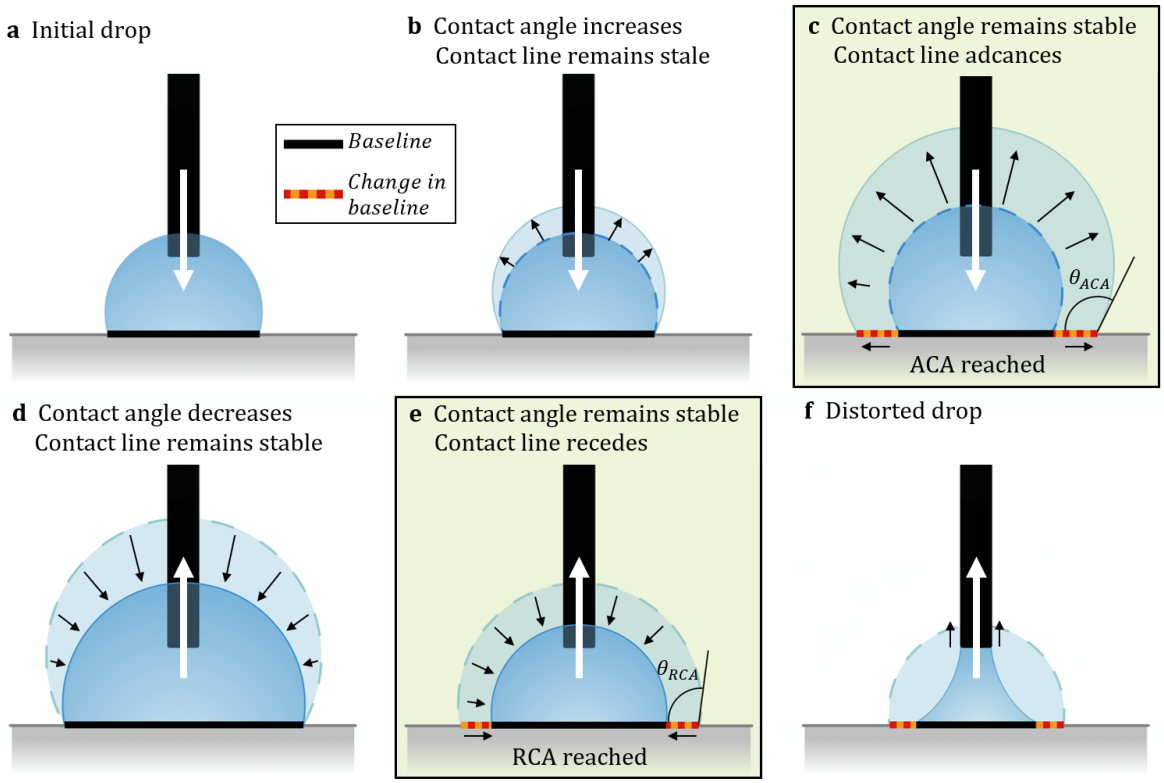

Figure 5.6: The stages of ACA and RCA measurement. **a**: An initial drop of 2 µL is deposited. **b**: Before measurement is started 1 µL water is added. ACA is not reached, baseline remains stable while the shape of the drop changes. **c**: ACA is reached. As the volume increases from 3 to 10 µL the baseline increases while CA remains stable. **d**: Water is first removed from an initial drop before RCA measurements are started. RCA is not necessarily reached, baseline remains stable as the shape of the drop changes. **e**: As the volume is decreased from 10 to 3 µL the baseline start to decrease, and the CA remains stable. **f**: Further decrease of the volume leads to a distorted drop due to the needle.

Chapter 6

Results and Analysis

This chapter presents the results and analysis achieved in this thesis work. First, an analysis of the AFM images of the samples is presented, followed by the freezing and wetting experiments results.

As mentioned in section 2.2.3, Eberle et al. [1] found from their experiments that surfaces with nanostructuring leads to the same extremely low freezing onset temperature of $\sim -24\,^{\circ}\mathrm{C}$ for over three orders of magnitude change in RMS size ($\sim$0.1 nm to $\sim$100 nm). This thesis studies five diamond samples with different surface roughness to confirm that the freezing onset temperature changes very little for nanostructured surfaces with different RMS roughness. One ultra-nanocrystalline sample labeled S1, three nanocrystalline diamond on silicon samples labeled S2-S4, and one microcrystalline sample labeled S5 were used.

An investigation of the samples' wetting and anti-icing properties was completed by measuring water contact angles, contact angle hysteresis, freezing onset temperatures, and freezing delays. The experiments were done in four cycles with 6-8 measurements for the water contact angle and freezing onset temperature measurements. Cycle 1 was done in low humidity with about 20-40 % relative humidity at $\sim 21\,^{\circ}\mathrm{C}$. In order to see if humidity influences wetting and icephobic properties, measurements in cycle 2 were done with high humidity of about 50-70 % relative humidity at $\sim 20\,^{\circ}\mathrm{C}$. The humidity changed a lot during each measurement; thus, measurements done in cycle 3 were done with a stable relative humidity of 40-50 % at $\sim 18\,^{\circ}\mathrm{C}$. The last measurements under cycle 4 were done in a closed system to ensure a constant atmosphere during the measurements. This setup closely resembles the setup used by Eberle et al. [1]. It was originally planned to do all measurements at the same humidity, but this was unfortunately not possible due to some problems with the lab infrastructure.

6.1 Surface Characterization

This thesis studied five diamond samples with different roughness. Including one ultra-nanocrystalline, three nanocrystalline, and one microcrystalline sample. The samples were fabricated by the nanophysics group at the University of Bergen (UiB) by Dr. Justas Zalieckas. Chemical vapor deposition (CVD) (described in section 3.2) was used to grow the diamond samples on silicon. All the samples are hydrogen-terminated, resulting in the nature of the CVD growth process. A detailed description of the fabrication process is beyond this thesis work.

The topography of the sample's surface was analyzed using the Atomic Force Microscopy (AFM)(see section 4.1), also done by the nanophysics group at UiB by Dr. Ranveig Flatabø. The AFM scans were performed in contact mode using a CSC17 tip and measured along the diagonal of the samples. Data visualization and analysis of the AFM scans were done using an AFM software called *Gwyddion*. The software was used to visualize the surface topography in 3D and measure the RMS roughness of the surface (see section 4.1.3). The results of the RMS roughness are given in table 6.1, where each value is the average of three images (one from the middle and two from the edges).

Table 6.1: RMS roughness of the diamond samples, measured by AFM. The values are calculated as an average of 3 measurements. Except for the microcrystalline sample S5, due to complications, was measured by a profilometer. Only one measurement was taken; therefore, approximately RMS roughness is given for sample S5.

	S1	**S2**	**S3**	**S4**	**S5**
RMS roughness [nm]	9 ± 3	18 ± 2	22 ± 4	56 ± 7	$\sim$530

Figure 6.1 shows the AFM image for the ultra-nanocrystalline sample S1 with a RMS roughness of 9±3 nm.

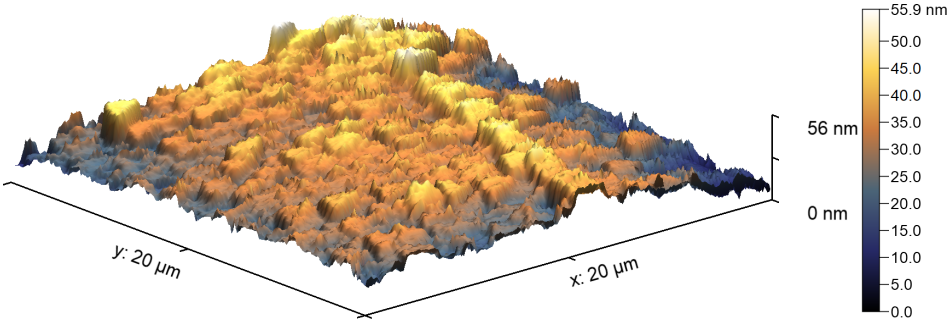

Figure 6.1: AFM image of the ultra-nanocrystalline sample S1.

Figure 6.2, 6.3 and 6.4 shows the nanocrystalline samples S2-4, with an RMS roughness of 18±2 nm, 22±4 nm, and 56±7 nm, given respectively. The ultra-nanocrystalline sample S1, as seen in the figures, is much smoother than the rest, with less distinguished

grains. The two nanocrystalline samples, S2 and S3, look similar, with well-defined grains and small differences in surface height and RMS roughness. Compared to the rest, the last nanocrystalline sample, S4, has much bigger grains. It also has a surface height ∼200 nm higher than the other nanocrystalline samples.

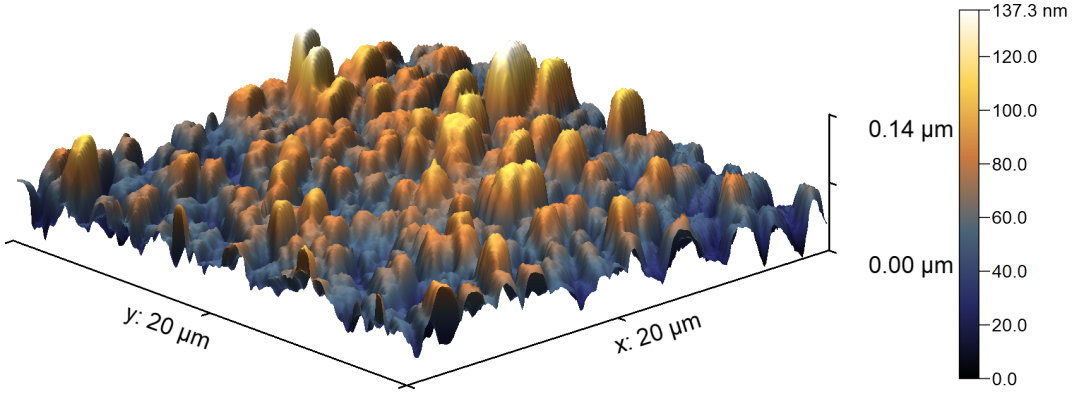

Figure 6.2: AFM image of the nanocrystalline sample S2.

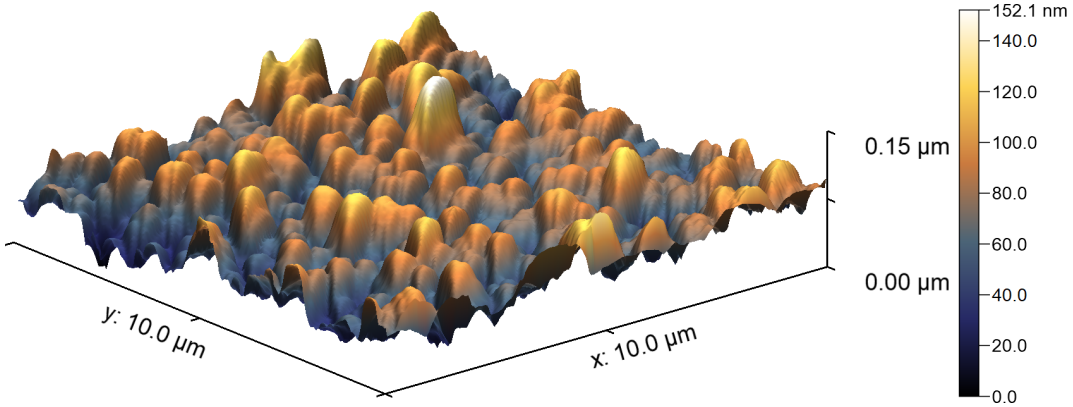

Figure 6.3: AFM image of the nanocrystalline sample S3.

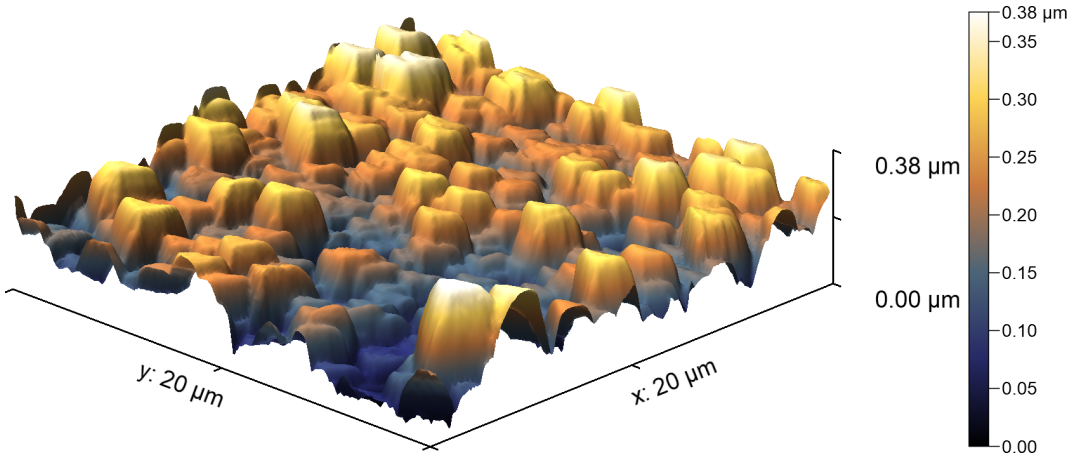

Figure 6.4: AFM image of the nanocrystalline sample S4.

Unfortunately, it was not possible to do an AFM analysis of the microcrystalline sample S5 due to the large roughness, and thus no images of the surface topography are presented. Instead, the sample is investigated with a profilometer by a collaborator of the nanophysics group at UiB. Only one measurement was taken, and thus difficult to estimate the uncertainty of the measurement. The sample is to be investigated further. However, due to time limitations, this was not done in this thesis. The RMS roughness of sample S5 was measured as approximately 0.53 µm by the profilometer as seen in figure 6.5.

Figure 6.5: Image of the Profilometer used to measure the roughness of the microcrystalline sample S5.

6.2 Freezing Onset Temperature Measurements

As stated at the beginning of this chapter, the freezing onset temperature experiments were done in four cycles with different relative humidities and 6-8 measurements per cycle. See section 5.2.1 for details of how the measurements were taken.

The freezing onset temperature is the temperature when freezing starts, and can be observed as a sudden change in the droplet's optical appearance, as the droplet appears hazy, as seen in the middle images in figure 6.6. The figure shows water droplet images for samples S1-S5 as the samples are cooled down until the droplets are frozen. The left-side images show the water droplets before freezing, the middle images are taken at the freezing onset, and the right-side images are taken after the droplet is completely frozen. The images are taken from measurements done at low relative humidity (cycle 1).

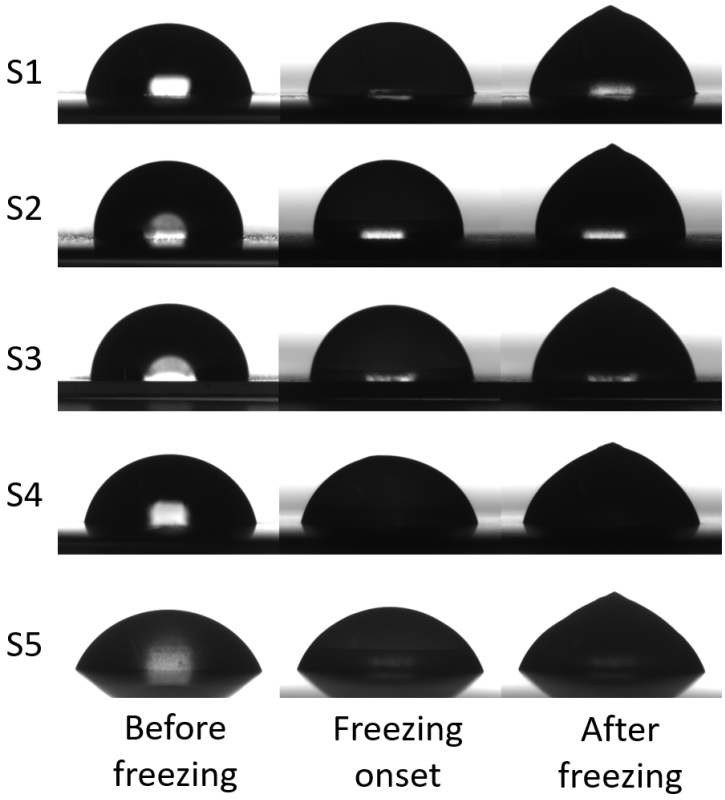

Figure 6.6: Images of water droplets (5 µL) on diamond samples with different roughness. Left images shows the droplets at room temperature, middle images are taken at the freezing onset, and right images taken after the droplets are completely frozen.

6.2.1 Cycle 1 - Low humidity (20-40% RH)

At cycle 1, the measurements was done with ambient temperature in the range 21-22 °C, and relative humidity about 20-40 %. The results of the freezing onset temperature measurements are presented in table 6.2, with the value being an average of all measurements.

The data are plotted as a box plot in figure 6.7. A box plot visually shows the data distribution through quartiles and median. The red line inside the box shows the median of the measured freezing onset temperature, the bottom and top line of the box represents the first and third quartile, which indicates where 25 % and 75 % of the data is below this point. The lower and upper whiskers show the minimum and maximum values.

From the experiments, it was found that all samples were exhibiting the same low freezing onset temperature of −21 °C to −22 °C. Thus, the freezing onset temperature changes minimally with a change in the RMS roughness, which is in good agreement with what Eberle et al. [1] reported.

Table 6.2: Results from the freezing onset temperature measurements at cycle 1 for sample S1-S5, with the average relative humidity and room temperature for the measurements, where each value is an average of 6-8 measurements.

Sample	RMS Roughness	Freezing Onset Temp	RH	Room Temp
S1	9 nm±3 nm	−21 °C±2 °C	32 %±2 %	21 °C±1 °C
S2	18 nm±2 nm	−22 °C±4 °C	32 %±1 %	21 °C±1 °C
S3	22 nm±4 nm	−21 °C±2 °C	39 %±1 %	21 °C±1 °C
S4	56 nm±7 nm	−22 °C±2 °C	22 %±2 %	21 °C±1 °C
S5	530 nm	−22 °C±2 °C	20 %±1 %	22 °C±1 °C

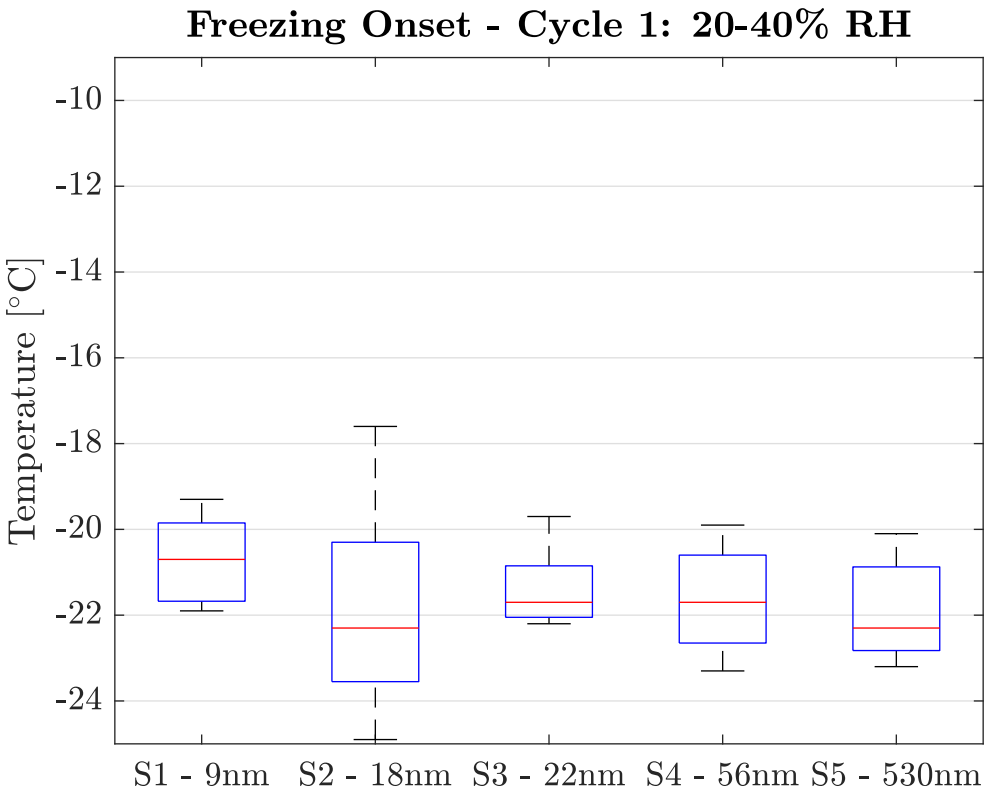

Figure 6.7: Measured freezing onset temperature for cycle 1 on samples S1-S5. The red line inside the box shows the median value. The box's bottom and top line represent the first and third quartile, which indicates where 25% and 75% of the data are below this point. Lower and upper whiskers are the minimum and maximum values.

6.2.2 Cycle 2 - High humidity (50-70% RH)

In the next cycle, the measurements were done with an ambient temperature of 20 °C, and relative humidity of 50-70 %. The results of the freezing onset temperature measurements from cycle 2 are presented in table 6.3, with the value being an average of

the measurements. A box plot of the data is shown in figure 6.8.

The freezing onset temperature differs more between the samples than in cycle 1. It indicates that a change in the RMS roughness in the nano range does affect the freezing onset temperature at higher RH, in contrast with the results from cycle 1. From table 6.3 one also sees that the freezing onset temperature is higher than the results for cycle 1 for all samples. The microcrystalline sample S5 went from a freezing onset temperature of $-22\,^{\circ}\mathrm{C}$ at low RH to $-12\,^{\circ}\mathrm{C}$ at high RH. This clearly indicates that the relative humidity in the room affects the measurements. However, the nanocrystalline samples S2 and S3 still exhibit low freezing onset temperature with an average of $-21\,^{\circ}\mathrm{C}\pm4\,^{\circ}\mathrm{C}$ and $-18\,^{\circ}\mathrm{C}\pm4\,^{\circ}\mathrm{C}$.

Note that the relative humidity in the room changed a lot during the measurements, which may explain the larger spread in data compared to the last cycle.

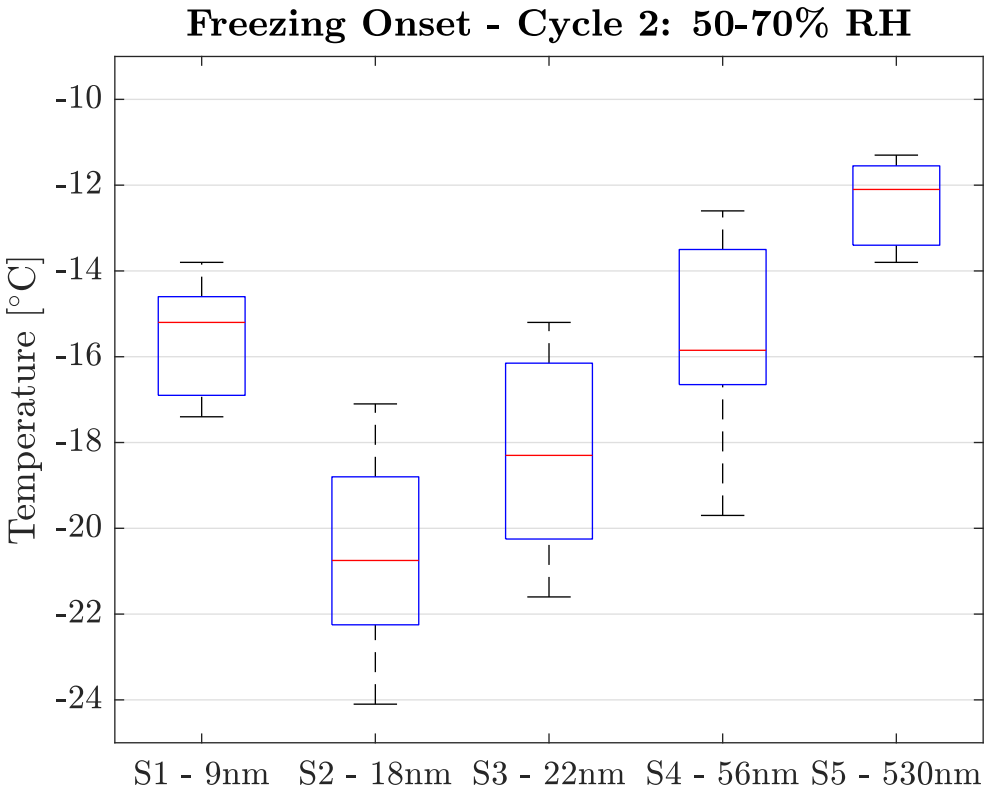

Figure 6.8: Measured freezing onset temperature for cycle 2 on the samples S1-S5. The red line inside the box shows the median value. The box's bottom and top line represent the first and third quartile, which indicates where 25% and 75% of the data are below this point. Lower and upper whiskers are the minimum and maximum values.

Table 6.3: Results from the freezing onset temperature measurements of cycle 2 for sample S1-S5, with the average relative humidity and room temperature for the measurements, where each value is an average of 6-8 measurements.

Sample	RMSRoughness	FreezingOnsetTemp	RH	RoomTemp
S1	9 nm±3 nm	−16 °C±2 °C	66 %±8 %	20 °C±1 °C
S2	18 nm±2 nm	−21 °C±4 °C	53 %±4 %	20 °C±1 °C
S3	22 nm±4 nm	−18 °C±4 °C	64 %±12 %	20 °C±1 °C
S4	56 nm±7 nm	−16 °C±4 °C	56 %±5 %	20 °C±1 °C
S5	530 nm	−12 °C±2 °C	66 %±8 %	20 °C±1 °C

6.2.3 Cycle 3 - Stable Humidity (40-50% RH)

Since the RH changed a lot during the measurements in cycle 2, a new set of measurements was done in a more stable RH. In cycle 3, the measurements was done with ambient temperature in the range 18 °C to 19 °C, and a relative humidity in the range 40-50 %. The results of the freezing onset temperature measurements from cycle 3 are presented in table 6.4, with the value being an average of the measurements. A box plot of the data is shown in figure 6.9.

From the plot, one can see a much larger spread in the data compared to the last cycles. Unlike cycle 2, the humidity is more stable, but still, there is much spread in the data. Comparing figure 6.7 from cycle 1 with figure 6.9 from cycle 3, it appears that the limit for when condensation start affecting the freezing process is around 40-50 % RH. Hence the large spread in data.

However, one still sees the same trend as cycle 2, with the nanocrystalline samples S2 and S3 having a low average freezing onset temperature of −20 °C±5 °C and −19 °C±5 °C, and the other samples having roughly 10 °C higher freezing onset temperature then cycle 1.

Table 6.4: Results from the freezing onset temperature measurements for cycle 3 on sample S1-S5, with the average relative humidity and room temperature for the measurements, where each value is an average of 6-8 measurements.

Sample	RMS Roughness	Freezing Onset Temp	RH	Room Temp
S1	9 nm±3 nm	−15 °C±4 °C	54 %±1 %	18 °C±1 °C
S2	18 nm±2 nm	−20 °C±5 °C	44 %±2 %	19 °C±1 °C
S3	22 nm±4 nm	−19 °C±5 °C	46 %±1 %	18 °C±1 °C
S4	56 nm±7 nm	−12 °C±3 °C	44 %±1 %	18 °C±1 °C
S5	530 nm	−12 °C±1 °C	44 %±1 %	18 °C±1 °C

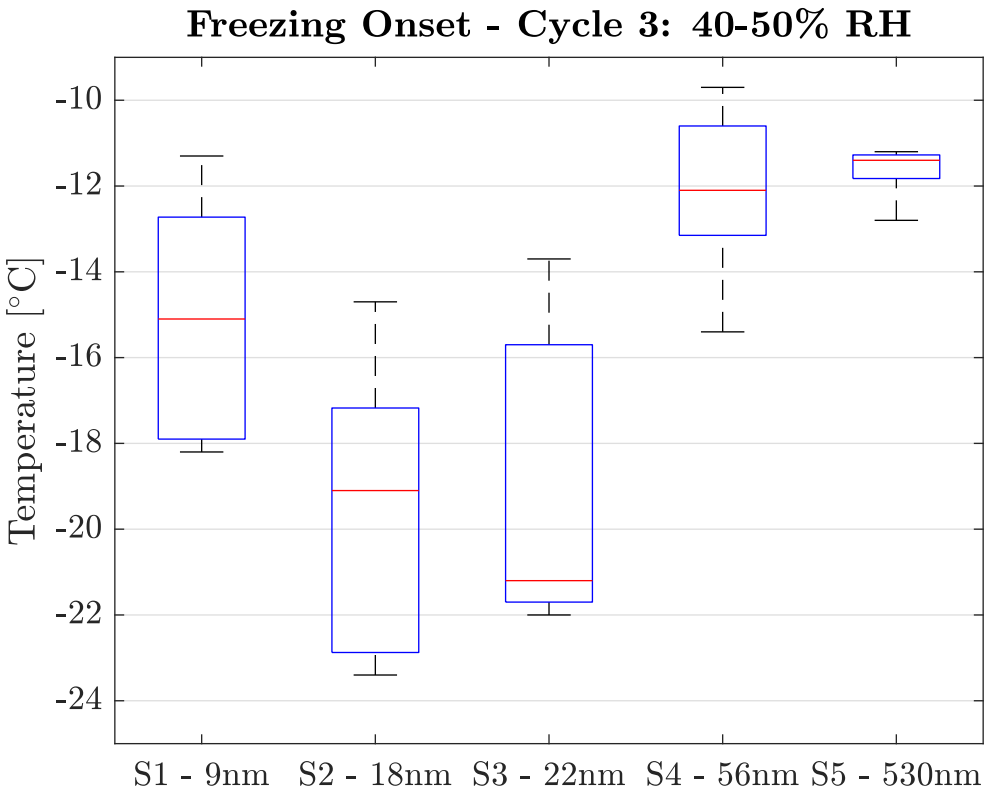

Figure 6.9: Measured freezing onset temperature for cycle 3 on samples S1-S5. The red line inside the box shows the median value. The box's bottom and top line represent the first and third quartile, which indicates where 25% and 75% of the data are below this point. Lower and upper whiskers are the minimum and maximum values.

6.2.4 Cycle 4 - Closed System

In the last cycle, the measurements were done in a closed box to ensure a constant atmosphere during the measurements and to repeat as closely as possible the setup used by Eberle et al. [1]. The results of the freezing onset temperature measurements from cycle 4 are presented in table 6.5, with the value being an average of 6-8 measurements. A box plot of the data is shown in figure 6.10. Any measurements with a significantly higher freezing onset temperature than the rest are defined as outliers and shown as red crosses. The outlier is caused by dust and impurities acting as nucleation sites, causing the droplet to freeze at higher temperatures.

The nanocrystalline samples S2-S4 were found to have a relatively constant freezing onset temperature, with values in the range $-21\,^{\circ}\mathrm{C}$ to $-22\,^{\circ}\mathrm{C}$, which is similar to what was found in cycle1 for these samples. The difference between cycles 1 and 4 was for the ultra-nanocrystalline and microcrystalline samples. However, the results are actually in good agreement with Eberle et al. [1]. They claim that there is very little change in

freezing onset temperature over a broad range of RMS roughness. However, this is only for nanostructured surfaces in the range 0.17-173 nm. Even though sample S1 has a nominal RMS roughness of around 9 nm, it is, in actual fact, atomically flat over large areas and so the local curvature in most places will be very large. The microcrystalline sample S5 is outside the Eberle roughness range, so one would expect both S1 and S5 to not exhibit the same low freezing onset temperature as the nanocrystalline samples. Then only looking at samples S2-S4, the freezing onset temperature is constant with a value around $-22\,^{\circ}\mathrm{C}$, in agreement with what was reported by Eberle et al. [1].

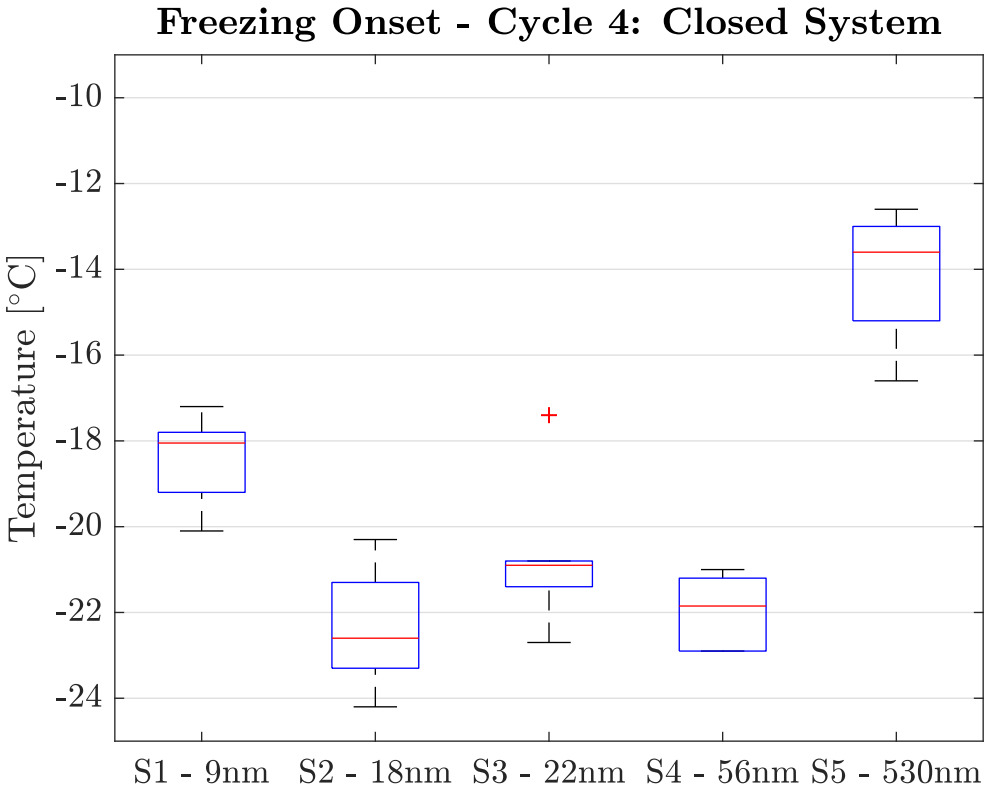

Figure 6.10: Measured freezing onset temperature for cycle 4 on the samples S1-S5. The red line inside the box shows the median value. The box's bottom and top line represent the first and third quartile, which indicates where 25% and 75% of the data are below this point. Lower and upper whiskers are the minimum and maximum values. Any outliers are shown as red crosses.

Table 6.5: Results from the freezing onset temperature measurements for cycle 4 on sample S1-S5, with the average relative humidity and room temperature for the measurements, where each value is an average of 6-8 measurements.

Sample	RMSRoughness	FreezingOnsetTemp	RH	RoomTemp
S1	9 nm±3 nm	−18 °C±2 °C	53 %±4 %	20 °C±1 °C
S2	18 nm±2 nm	−22 °C±2 °C	40 %±4 %	23 °C±1 °C
S3	22 nm±4 nm	−21 °C±3 °C	39 %±3 %	22 °C±2 °C
S4	56 nm±7 nm	−22 °C±1 °C	52 %±3 %	20 °C±1 °C
S5	530 nm	−14 °C±2 °C	39 %±1 %	22 °C±1 °C

6.3 Freezing Delay

Freezing delay measurements are shown in figure 6.11. Note that these measurements are done in a closed system, with similar conditions as cycle 4 of the freezing onset measurements. The results are in reasonable agreement with the freezing onset measurements, as the ultra-nano and microcrystalline samples S1 and S5 did not reach a temperature of −20 °C before freezing. However, the freezing delay measurements show a much larger spread in the measured data than the freezing onset measurements. For example, for the microcrystalline sample S5, at −10 °C the freezing delay was 100 min at the longest and a couple of minutes at the shortest. It is not quite clear why this is. A possible effect may be that early freezing onset is triggered by impurities on the surface, such as dust or possible imperfections in the coating. This will have to be investigated in future work. Eberle et al. [1] predict freezing delays of ∼25 hours at −21 °C for their samples.

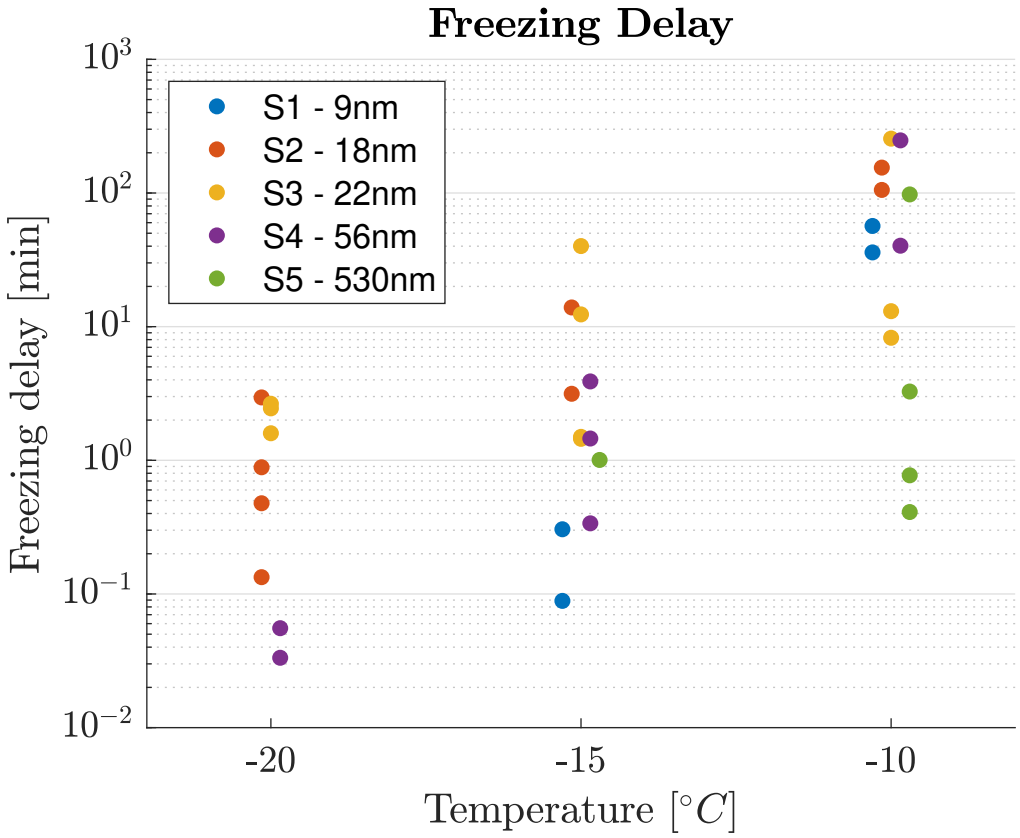

Figure 6.11: Freezing delay measurements for the diamond samples S1-S5 on three different temperatures: −20 °C, −15 °C, and −10 °C.

6.4 Water Contact Angle (WCA)

The WCA was measured to determine the wettability of each sample. As mentioned in section 2.2.3, Eberle et al. [1] used both hydrophilic and hydrophobic samples in their experiments. However, no change in freezing onset temperature was observed regardless of the different wettabilities. The WCA is thus measured to discuss if it affects the anti-icing results in this thesis.

Figure 6.12 shows images of a water droplet (5 µL) on the ultra-nanocrystalline diamond sample S1, the nanocrystalline diamond samples S2-S4, and on the microcrystalline diamond sample S5 for all cycles. The images are taken at room temperature. The results of the water contact angles for the droplets on each sample at room temperature are given in table 6.6, with the values being an average of 6-8 measurements on each cycle.

With a relative humidity of 20-40% (cycle 1), the nanocrystalline sample S2 was found to be hydrophobic at room temperature (90°±7°). Overall, all of the nanocrystalline sam-

ples S2-S4 were found to be close to hydrophobic at room temperature with WCA above 80°. The ultra-nanocrystalline and microcrystalline samples exhibit less hydrophobicity, with a WCA of 76°±6° for S1 and 70°±7° for S5.

Table 6.6: Water contact angles for droplets on the diamond samples S1-S5 at room temperature, where each value is an average of 6-8 measurements per cycle.

Sample	Cycle1	Cycle2	Cycle3	Cycle4
S1 - 9nm	76°±6°	67°±5°	63°±5°	62°±2°
S2 - 18nm	90°±7°	80°±3°	77°±1°	70°±7°
S3 - 22nm	86°±3°	80°±5°	79°±3°	77°±4°
S4 - 56nm	81°±4°	71°±4°	61°±4°	65°±3°
S5 - micro	70°±7°	68°±5°	58°±4°	65°±5°

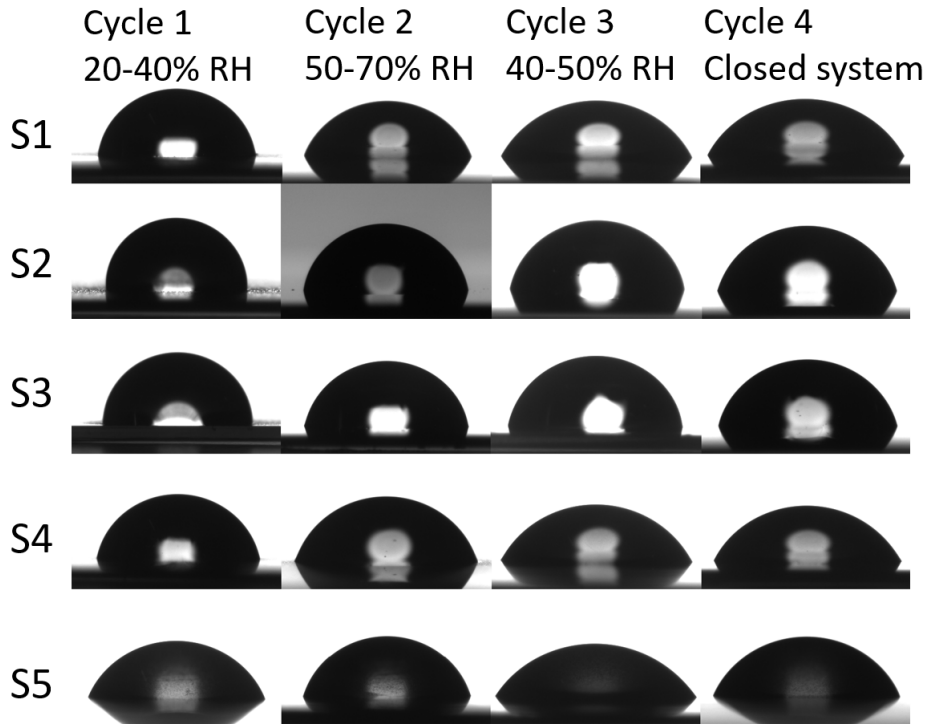

Figure 6.12: Images of water droplets (5 µL) on diamond samples with different roughness. Images are taken at room temperature.

6.4.1 Advancing and Receding Contact Angle

As previously mentioned in section 2.1.3, measurements of the static CA (like the measurements of the WCA done in the section above) are not necessarily reproducible due to CAH. Thus, the ACA and RCA should also be measured to characterize the sample's wettability properly. However, as mentioned in the procedure in section 5.3.2,

measuring the RCA can be challenging, as the initial volume drop may need to be surprisingly large to achieve a reliable result. If the initial drop volume is too small, the CA fails to reach equilibrium before the instrument is finished withdrawing water from the drop.

As explained in the procedure (section 5.3.2) before starting the RCA measurements, a test measurement was done to find the initial drop volume size for each sample. RCA measurements with the initial drop size were then done. However, the measurements failed to reach RCA before all water was withdrawn. Both larger and smaller drop size was also tested. For instance, figure 6.13 shows one of the RCA measurements on sample S1, and figure 6.14 shows RCA measurements for sample S5. As the baseline decreases, an approximately constant RCA should be found. This was not found in the measurements done in this thesis, as seen in the figures.

After the measurements were taken, it was discovered that the humidifier for the cleanroom the experiments were done in did not work properly, which most possibly affected the results. For instance, there was a large change in the ARCA measurements from the measurements taken when the humidifier did not work compared to the measurement taken when it worked. Figure 6.14a shows ARCA measurement on sample S5 before the humidifier stop working, and figure 6.14b for sample S5 with broken humidifier. Both the ACA and the RCA are reached for the measurements with a working humidifier. The measurements taken with a broken humidifier also exhibited lower CAs for both ACA and RCA. It was then concluded that the humidity in the room was the reason for not achieving reliable results. Unfortunately, the author had only done one measurement on sample S5 with a working humidifier. Thus due to the broken humidifier and time limit, no new reliable measurement of the ARCA was taken.

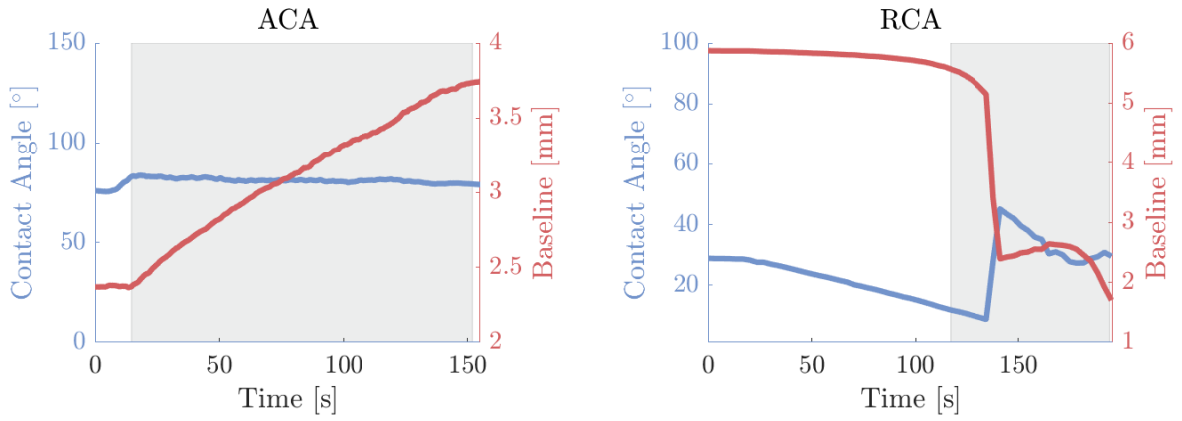

Figure 6.13: ACA (left) and RCA (right) measurement on sample S1. The marked grey area shows when the baseline is increasing or decreasing, thus when the drop is advancing or receding, i.e. the ARCAs.

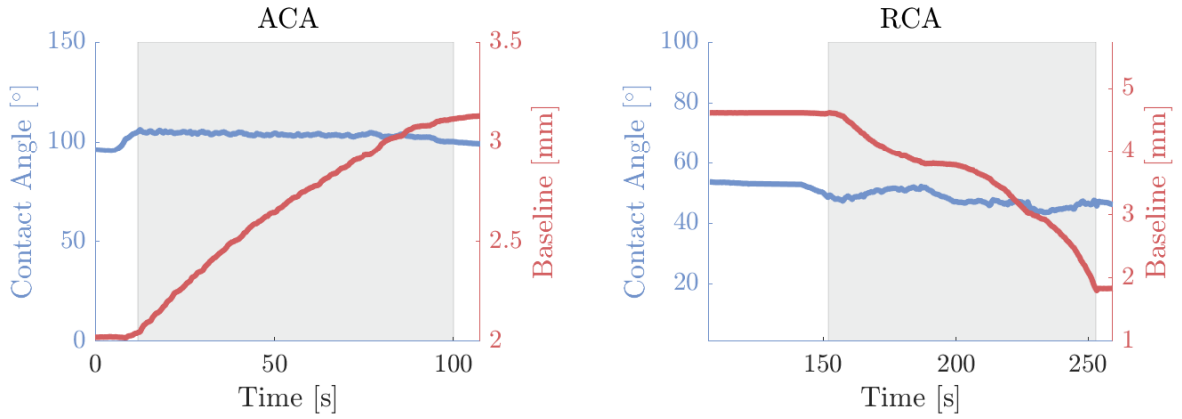

(a) ARCA measurements done with working humidifier.

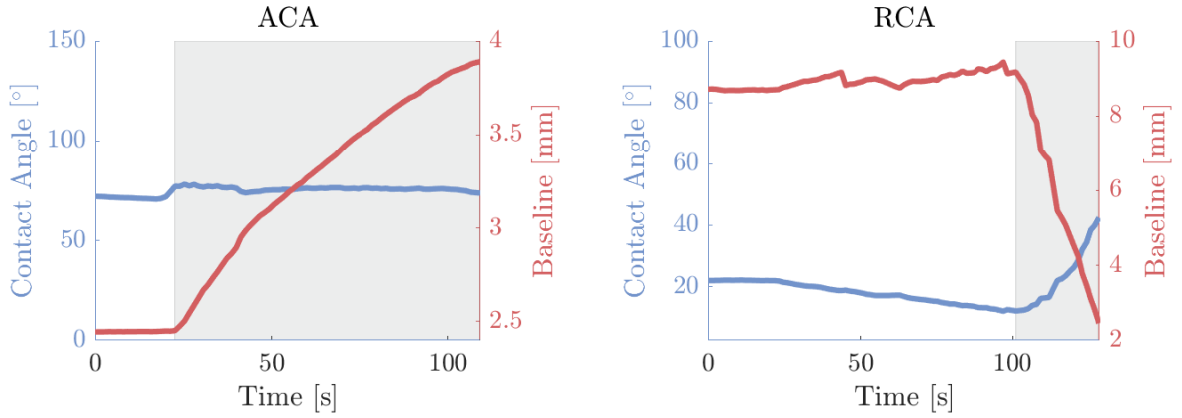

(b) ARCA measurements done with broken humidifier.

Figure 6.14: ACA (left) and RCA (right) for measurement on sample S5. **a)** shows an ARCA measurement done when the humidifier in the room worked, and **b)** when the humidifier did not work. The marked grey area shows when the baseline increases or decreases, thus when the drop is advancing or receding, i.e., the ARCAs.

Chapter 7

Discussion

This chapter discusses the result of this thesis work and some reflections on related work found in the literature.

One of the main discussions in this thesis is the influence of surface roughness on wetting and anti-icing properties. As described in section 2.2, the classical nucleation theory (CNT) states that the roughness of a surface affects the free energy barrier for surface roughness radius $R < 10r^*$. Note that R is not the same as the RMS value, and an analysis of the curvature distribution on the sample is needed instead. Regardless, CNT states that ice nucleation on smoother surfaces such as the ultra-nanocrystalline sample is more affected by the roughness than rougher samples like the microcrystalline sample. However, Eberle et al. [1] (see the section 2.2.3 for details) postulated that a change in the ice nucleus CA due to a quasi-liquid layer counteracted the roughness effect for nanostructured surfaces. Experimental results revealed a constant freezing onset temperature for over three orders of magnitude in RMS roughness ($\sim$0.2 to $\sim$100 nm).

7.1 Anti-Icing Properties of Diamond Surface

The anti-icing properties of the diamond surfaces were mainly measured through freezing onset temperature and freezing delay measurements. The first set of measurements of the freezing onset temperatures (cycle 1) was taken with a RH of 20-40 %. The results did not agree with the CNT, supporting the hypothesis that there is a quasi-liquid layer between the ice nuclei and the surface as postulated by Eberle et al. [1].

The last measurements were done in a closed system using an environmental chamber (cycle 4), similar to how Eberle et al. [1] measurements were taken under a condition of saturated humidity with respect to ice in order to avoid evaporation effects. The ultra-nanostructured sample S1 and microcrystalline sample S5 have a higher freezing

onset value than the nanostructured samples. Even though sample S1 has a nominal RMS roughness of around 9 nm, it is essentially completely flat on the atomic scale over large areas. The local curvature in most places will be very large. As explained in section 2.2.3, the change of θ_{IW}, due to the quasi-liquid layer, counteracts the roughness-dependent ice nucleation promotion in nanopits estimated by the classical nucleation theory. Nucleation on flatter regions with a curvature radius $R > 10r^*$ then becomes dominant, explaining why the ultra-nanocrystalline sample S1 has a slightly larger freezing onset temperature. The microcrystalline sample S5 also exhibits large local curvatures, as it has large slops that are atomically flat. Therefore, both S1 and S5 are expected to have a higher freezing onset temperature, in good agreement with Eberle et al. [1].

The freezing delay measurements show a much larger spread in the measured data than freezing onset. For example, the microcrystalline sample S5, at $-10\,^{\circ}\mathrm{C}$ had a freezing delay time of 100 min at the longest and a couple of minutes at the shortest. The possible reasoning for this could be due to dust particles on the surface, which can promote heterogeneous nucleation in the droplet. However, the freezing onset measurements did not appear to be impacted. An increasing frost formation could also be a factor to consider, as the freezing delay measurements span several minutes to hours while freezing onset measurements only last 2-5 minutes. Additionally, disturbances, such as vibrations, greatly impact the measurements. On multiple occasions, the droplets started to freeze right after the door to the cleanroom was closed or the table the instrument stood on was barely moved. Thus, the sample may exhibit a longer freezing delay time than seen in this thesis.

7.1.1 Environmental Effects on Anti-Icing and Wetting

However, as the RH was changed in the following cycles, the results deviate even further from Eberle et al. [1]. Figure 7.1 shows the freezing onset temperature for all cycles plotted by relative humidity. In figure 7.1a, the colors indicate the different samples, and in figure 7.1b, the color indicates the different cycles. The figure shows that the droplets start freezing at higher temperatures when RH is higher. As mentioned under section 6.2.3, the limit where RH starts affecting the freezing process is around 40-50 %. This can be seen in figure 7.1b, where all measurements from cycle 1 have a freezing onset temperature of $\sim -20\,^{\circ}\mathrm{C}$ or below. However, when the RH is 40-50 % (cycle 3), the freezing onset temperatures are found to be as high as $-10\,^{\circ}\mathrm{C}$ for some of the samples. From figure 7.1a, the nanocrystalline samples S2-S3 are found to be less affected by the increase in RH. Note that due to the unstable humidity during cycle 2, measurements were taken at different humidities for some samples. E.g., measurements on sample S2 were done in 60 RH at the highest, while samples S1 and S5 have measurements in RH above 70 %. This is seen in figure 7.1a.

It is then concluded that the anti-icing properties of the diamond surface depend on

RH. Possible explanations could be due to the surfaces experiencing higher wettability at higher RHs, as seen in the WCA measurements. As described in section 2.2.1, the CNT states that ice nucleation depends on roughness and possible nucleation sites, where the latter increases with increasing wettability. Explains why samples S2 and S3 delay freezing better, as the WCA (see table 6.6) was larger than the other samples. Wang et al. [59] investigated the spreading of liquid under various RH levels. They found that increasing RH reduced the static CA of the liquid droplets due to adsorbed water creating a precursor film on the surface, revealed by AFM. They also observed that the liquid droplets take on a minimum static CA at ∼70 % RH, at which the surface was fully covered by water molecules shown by AFM imaging. Tavakoli et al. [60] also showed an increase in the spreading of water droplets on a cooled surface due to increasing RH. These experiments were not done on diamond surfaces. However, it is reasonable to assume that an increase in RH enhances the formation of water film on the diamond surface as a decrease in the WCA is seen.

However, as mentioned in section 2.2.3, Eberle et al. [1] tested both hydrophobic and hydrophilic samples, ranging from a CA of $\sim 150^{\circ}$ to complete wetting and still got a constant freezing onset. Similar to the result in cycle 4, approximately constant freezing onset (except for the microcrystalline sample S5) but still higher wetting than in low humidity. However, these measurements are done in a closed system with a saturated atmosphere to avoid evaporation. Jung et al. [61] found that environmental conditions had a significant impact on the icephobicity of surfaces. They demonstrated that humidity and the surrounding gas flow could switch the ice crystallization mechanism. A supercooled water droplet in an unsaturated gas will undergo evaporation, which reduces the liquid temperature locally at the gas-liquid interface. The reduction in temperature could enhance homogeneous nucleation. However, homogeneous nucleation was unlikely to initiate freezing on this thesis samples, as freezing of water droplets began at the surface and not at the liquid-vapor interface. The effects of evaporation in this thesis work remain unknown. However, it can be a potential explanation for why samples in unsaturated humidities (cycles 2 and 3) freeze at a lower temperature than cycle 4 (with saturated humidity), regardless of the approximately same WCA.

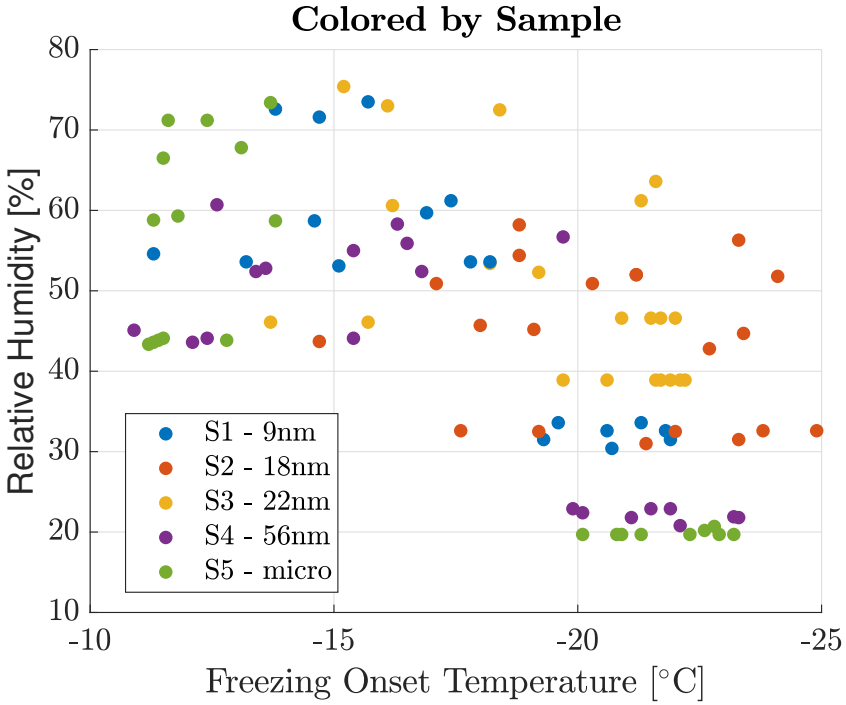

(a) Colors of the circles indicate different samples.

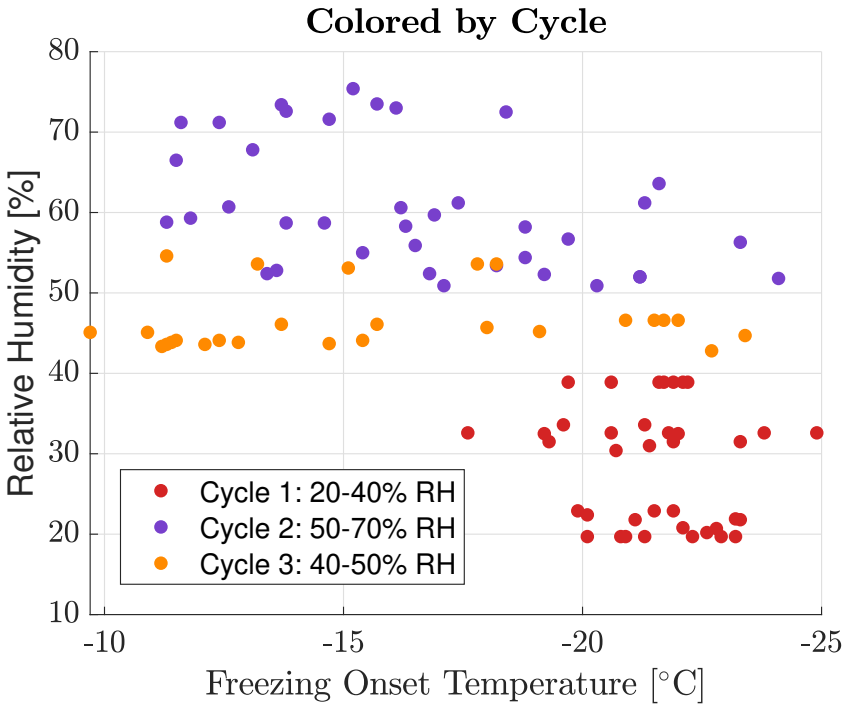

(b) Colors of the circles indicate different cycles.

Figure 7.1: Plot shows the freezing onset temperature vs relative humidity for all samples.

7.2 Surface Topography and Chemistry

The AFM analysis of the diamond samples showed the different grain sizes the samples have. As described in section 3.2.1, in order to grow ultra-nanocrystalline samples, re-nucleation of the diamond grains is needed. The grains grow closer together and are less distinguishable, clearly seen in the ultra-nanocrystalline sample S1. The re-nucleation also generates a higher sp^2 carbon bonding at the grain boundaries. Williams et al. [44] stated that UNCD exhibits amorphous grain boundaries similar to diamond-like-carbon (DLC), which has no crystalline structure. Moreover, the UNCDs small grain sizes increase the grain boundary volume fraction and the amount of non-diamond carbon. Thus, UNCD film properties tend to deviate more considerably from bulk diamond properties than films with higher sp^3 bonds.

Chapter 8

Conclusion and Future Work

In this thesis, the objective has been to investigate the anti-icing properties of diamond surfaces with different roughness. Five samples grown by CVD were studied, all hydrogen-terminated. Including one ultra-nanocrystalline, three nanocrystalline, and one microcrystalline diamond sample. The anti-icing and wetting properties were studied by measuring the freezing onset temperature, freezing delay times, and WCA. The results were then compared to an article by Eberle et al. [1], discussing how roughness influences the anti-icing properties. This thesis work also explored the impact of RH on the experiments.

The author concluded that the results agree with the new theoretical model and experimental results of Eberle et al. [1]. Furthermore, the diamond samples exhibit excellent anti-icing properties, with freezing onset temperatures of approximately $-22\,^{\circ}\mathrm{C}$ at low RH (20-40 %).

When the environmental conditions were changed, the results started to differ strongly from the Eberle et al. [1] results. Several measurements were also taken at high unsaturated RH of 40-50 % and 50-70 %, were a constant freezing onset was no longer detected. A change in both wettability and freezing onset temperature was seen for all samples. It was thus concluded that the RH drastically affects anti-icing properties.

The freezing delay measurements showed a large spread in the results, primarily due to disturbance of the setup as vibration initialized freezing. Other factors to consider are dust particles and frost formation on the surface. Due to time limitations, only a few measurements were completed for each sample, and a new set of freezing delay measurements should be taken.

In addition, the measurement of the contact angle hysteresis was not completed in this thesis due to time limitations and problems with the equipment. New measurements of the advancing and receding contact angle should therefore be taken to investigate the contact angle hysteresis of the samples.

The sample characterization of the microcrystalline sample S5 was also not completed. Due to large roughness, AFM imaging of the sample was not achieved. Thus the sample is to be investigated in future work by another microscopy that's not limited by roughness.

There is plenty of available research on anti-icing surfaces for various substrates. However, humidity's effect on icephobicity is often not considered, although harsh environments are present in many anti-icing applications. For the possibility of implementing anti-icing surfaces in commercial use, more research should be carried out. First, the freezing onset measurements should be done in a stable environment with high humidity. As some of the measurement carried out in this thesis was taken at an unstable humidity ranging from 50-70 % RH, which resulted in the measurements taken at different RH for each sample.

The gas flow of the surrounding environment is also naturally present in many anti-icing applications. Thus suggestions for future studies could be to investigate the effect of airflow on the freezing process, as done by Jung et al. [61]. Who showed that the gas flow dramatically affects the icephobicity of a surface due to an enhancement in homogeneous nucleation resulting in initializing the freezing process.

Bibliography

[1] P. Eberle, M. K. Tiwari, T. Maitra, and D. Poulikakos, "Rational nanostructuring of surfaces for extraordinary icephobicity," *Nanoscale*, vol. 6, pp. 4874–4881, 2014.

[2] J. Laforte, M. Allaire, and J. Laflamme, "State-of-the-art on power line de-icing," *Atmospheric Research*, vol. 46, no. 1, pp. 143–158, 1998.

[3] R. W. Gent, N. P. Dart, and J. T. Cansdale, "Aircraft icing," *Phil. Trans. R. Soc. Lond., A*, vol. 358, pp. 2873–2911, 2000.

[4] N. Dalili, A. Edrisy, and R. Carriveau, "A review of surface engineering issues critical to wind turbine performance," *Renewable and Sustainable Energy Reviews*, vol. 13, no. 2, pp. 428–438, 2009.

[5] C. C. Ryerson, "Ice protection of offshore platforms," *Cold Regions Science and Technology*, vol. 65, no. 1, pp. 97–110, 2011. Anti-Icing and De-Icing Techniques.

[6] O. Parent and A. Ilinca, "Anti-icing and de-icing techniques for wind turbines: Critical review," *Cold Regions Science and Technology*, vol. 65, no. 1, pp. 88–96, 2011. Anti-Icing and De-Icing Techniques.

[7] L. B. Boinovich and A. M. Emelyanenko, "Anti-icing potential of superhydrophobic coatings," *Mendeleev Communications*, vol. 23, no. 1, pp. 3–10, 2013.

[8] P. Hao, C. Lv, and X. Zhang, "Freezing of sessile water droplets on surfaces with various roughness and wettability," *Applied Physics Letters*, vol. 104, p. 161609, apr 2014.

[9] N. Akhtar, G. Anemone, D. Farias, and B. Holst, "Fluorinated graphene provides long lasting ice inhibition in high humidity," *Carbon*, vol. 141, pp. 451–456, 2019.

[10] P. Irajizad, S. Nazifi, and H. Ghasemi, "Icephobic surfaces: Definition and figures of merit," *Advances in Colloid and Interface Science*, vol. 269, pp. 203–218, apr 2019.

[11] A. Alizadeh, M. Yamada, R. Li, W. Shang, S. Otta, S. Zhong, L. Ge, A. Dhinojwala, K. R. Conway, V. Bahadur, A. J. Vinciquerra, B. Stephens, and M. L. Blohm, "Dynamics of ice nucleation on water repellent surfaces," *Langmuir*, vol. 28, pp. 3180–3186, jan 2012.

[12] K. K. Varanasi, T. Deng, J. D. Smith, M. Hsu, and N. Bhate, "Frost formation and ice adhesion on superhydrophobic surfaces," *Applied Physics Letters*, vol. 97, p. 234102, dec 2010.

[13] L. Cao, A. K. Jones, V. K. Sikka, J. Wu, and D. Gao, "Anti-icing superhydrophobic coatings," *Langmuir*, vol. 25, no. 21, pp. 12444–12448, 2009.

[14] S. Jung, M. Dorrestijn, D. Raps, A. Das, C. M. Megaridis, and D. Poulikakos, "Are superhydrophobic surfaces best for icephobicity?," *Langmuir*, vol. 27, pp. 3059–3066, feb 2011.

[15] L. Valentini and M. A. Lopez-Manchado, "Chapter 1 - classification of rubbers and components for harsh environmental systems," in *High-Performance Elastomeric Materials Reinforced by Nano-Carbons* (L. Valentini and M. A. Lopez Manchado, eds.), pp. 1–14, Elsevier, 2020.

[16] E. Y. Bormashenko, *Wetting of Real Surfaces*, ch. 2-4. De Gruyter, oct 2018.

[17] K.-Y. Law and H. Zhao, *Surface Wetting*, ch. 3-4. Springer International Publishing, 2016.

[18] G. M. Kontogeorgis and S. Kiil, *Introduction to Applied Colloid and Surface Chemistry*, ch. 1-2. John Wiley & Sons, Ltd, apr 2016.

[19] K. Mittal, ed., *Advances in Contact Angle, Wettability and Adhesion*, ch. 1. John Wiley & Sons, Inc., feb 2018.

[20] G. S. Selvaduray and R. Brindos, "*Effect of Temperature on Wetting Angle*," *National Educators' Workshop: Update 96 - Standard Experiments in Engineering Materials Science and Technology, NASA Publication*, vol. 3354, pp. 137–151, 1997.

[21] T. Young, "III. an essay on the cohesion of fluids," *Philosophical Transactions of the Royal Society of London*, vol. 95, pp. 65–87, dec 1805.

[22] N. Gao and Y. Yan, "Modeling superhydrophobic contact angles and wetting transition," *Journal of Bionic Engineering*, vol. 6, pp. 335–340, dec 2009.

[23] W. M. Sigmund and S.-H. Hsu, *Cassie–Baxter Model*, pp. 310–311. Berlin, Heidelberg: Springer Berlin Heidelberg, 2016.

[24] R. N. Wenzel, "RESISTANCE OF SOLID SURFACES TO WETTING BY WATER," *Industrial & Engineering Chemistry*, vol. 28, pp. 988–994, aug 1936.

[25] A. B. D. Cassie and S. Baxter, "Wettability of porous surfaces," *Trans. Faraday Soc.*, vol. 40, pp. 546–551, 1944.

[26] T. Huhtamäki, X. Tian, J. T. Korhonen, and R. H. A. Ras, "Surface-wetting characterization using contact-angle measurements," *Nature Protocols*, vol. 13, pp. 1521–1538, jul 2018.

[27] L. Gao and T. J. McCarthy, "Contact angle hysteresis explained," *Langmuir*, vol. 22, pp. 6234–6237, jun 2006.

[28] S. Karthika, T. K. Radhakrishnan, and P. Kalaichelvi, "A review of classical and nonclassical nucleation theories," *Crystal Growth & Design*, vol. 16, pp. 6663–6681, oct 2016.

[29] H. Vehkamäki, *Classical Nucleation Theory in Multicomponent Systems*. Springer Berlin Heidelberg, 2006.

[30] G. W. Lee, "Formation of metastable crystals from supercooled, supersaturated, and supercompressed liquids: Role of crystal-liquid interfacial free energy," *Crystals*, vol. 7, p. 326, oct 2017.

[31] V. Kalikmanov, *Nucleation Theory*. Springer Netherlands, 2013.

[32] X. Y. Liu, "Heterogeneous nucleation or homogeneous nucleation?," *The Journal of Chemical Physics*, vol. 112, no. 22, pp. 9949–9955, 2000.

[33] P. G. Vekilov, "Nucleation," *Crystal Growth & Design*, vol. 10, no. 12, pp. 5007–5019, 2010. PMID: 21132117.

[34] N. Maeda, "Brief overview of ice nucleation," *Molecules*, vol. 26, p. 392, jan 2021.

[35] N. H. Fletcher, "Size effect in heterogeneous nucleation," *The Journal of Chemical Physics*, vol. 29, pp. 572–576, sep 1958.

[36] G. Heydari, E. Thormann, M. Järn, E. Tyrode, and P. M. Claesson, "Hydrophobic surfaces: Topography effects on wetting by supercooled water and freezing delay," *The Journal of Physical Chemistry C*, vol. 117, no. 42, pp. 21752–21762, 2013.

[37] R. P. Sear, "Nucleation: theory and applications to protein solutions and colloidal suspensions," *Journal of Physics: Condensed Matter*, vol. 19, p. 033101, jan 2007.

[38] T. M. Schutzius, S. Jung, T. Maitra, P. Eberle, C. Antonini, C. Stamatopoulos, and D. Poulikakos, "Physics of icing and rational design of surfaces with extraordinary icephobicity," *Langmuir*, vol. 31, pp. 4807–4821, nov 2015.

[39] P. Faraday, "Xxiv. on regelation, and on the conservation of force," *The London, Edinburgh, and Dublin Philosophical Magazine and Journal of Science*, vol. 17, no. 113, pp. 162–169, 1859.

[40] R. R. Vanfleet and J. Mochel, "Thermodynamics of melting and freezing in small particles," *Surface Science*, vol. 341, no. 1, pp. 40–50, 1995.

[41] H. O. Pierson, *Handbook of Carbon, Graphite, Diamonds and Fullerenes*. Oxford: William Andrew Publishing, 1993.

[42] B. Wen, J. J. Zhao, and T. J. Li, "Synthesis and crystal structure of n-diamond," *International Materials Reviews*, vol. 52, no. 3, pp. 131–151, 2007.

[43] P. Hofmann, *Solid State Physics: An Introduction*. Wiley-VCH Verlag GmbH & Co, 2015.

[44] O. Williams, "Nanocrystalline diamond," *Diamond and Related Materials*, vol. 20, no. 5, pp. 621–640, 2011.

[45] A. K. Kulkarni, "Growth of diamond thin films by chemical vapour deposition," *Bulletin of Materials Science*, vol. 17, pp. 1379–1391, 1994.

[46] H. O. Pierson, *HANDBOOK OF CHEMICAL VAPOR DEPOSITION (CVD)*. Noyes Publications, 1999.

[47] K. Choy, "Chemical vapour deposition of coatings," *Progress in Materials Science*, vol. 48, no. 2, pp. 57–170, 2003.

[48] G. Cicala, P. Bruno, F. Bénédic, F. Silva, K. Hassouni, and G. Senesi, "Nucleation, growth and characterization of nanocrystalline diamond films," *Diamond and Related Materials*, vol. 14, no. 3, pp. 421–425, 2005. Proceedings of Diamond 2004, the 15th European Conference on Diamond, Diamond-Like Materials, Carbon Nanotubes, Nitrides and Silicon Carbide.

[49] Z. Liu, B. Zong, and Z. Lin, "Diamond growth on porous silicon by hot-filament chemical vapor deposition," *Thin Solid Films*, vol. 254, no. 1, pp. 3–6, 1995.

[50] M. N. R. Ashfold, P. W. May, C. A. Rego, and N. M. Everitt, "Thin film diamond by chemical vapour deposition methods," *Chem. Soc. Rev.*, vol. 23, pp. 21–30, 1994.

[51] J. Gracio, Q. Fan, and J. Mendes, "Diamond growth by chemical vapour deposition," *Journal of Physics D: Applied Physics*, vol. 43, p. 374017, sept 2010.

[52] M. Frenklach, "The role of hydrogen in vapor deposition of diamond," *Journal of Applied Physics*, vol. 65, pp. 5142–5149, jun 1989.

[53] O. Williams, M. Nesladek, M. Daenen, S. Michaelson, A. Hoffman, E. Osawa, K. Haenen, and R. Jackman, "Growth, electronic properties and applications of nanodiamond," *Diamond and Related Materials*, vol. 17, no. 7, pp. 1080–1088, 2008. Proceedings of Diamond 2007, the 18th European Conference on Diamond, Diamond-Like Materials, Carbon Nanotubes, Nitrides and Silicon Carbide.

[54] G. Haugstad, *Atomic Force Microscopy*. John Wiley & Sons, Inc., aug 2012.

[55] B. Voigtländer, *Atomic Force Microscopy*. Springer International Publishing, 2019.

[56] M. Lanza, ed., *Conductive Atomic Force Microscopy*. Wiley-VCH Verlag GmbH & Co. KGaA, oct 2017.

[57] Y. Leng, *Materials Characterization*. Wiley-VCH Verlag GmbH & Co. KGaA, sep 2013.

[58] Dataphysics-instruments, "Oca - optical contact angle measuring and contour analysis systems." https://www.dataphysics-instruments.com/products/oca/.

[59] Z. Wang, F. Shi, and C. Zhao, "Humidity-accelerated spreading of ionic liquids on a mica surface," *RSC Adv.*, vol. 7, pp. 42718–42724, 2017.

[60] F. Tavakoli and H. P. Kavehpour, "Cold-induced spreading of water drops on hydrophobic surfaces," *Langmuir*, vol. 31, no. 7, pp. 2120–2126, 2015.

[61] S. Jung, M. K. Tiwari, N. V. Doan, and D. Poulikakos, "Mechanism of supercooled droplet freezing on surfaces," *Nature Communications*, vol. 3, jan 2012.